SYNTHESIS OF MODIFIED NICKEL IRON LAYERED DOUBLE HYDROXIDES TO ENHANCE

ELECTROCHEMICAL PROPERTIES FOR SUPERCAPACITOR

Miss Machima Mongkhonratanachai

จุฬาลงกรณ์มหาวิทยาลัย

CHULALONGKORN UNIVERSITY

A Thesis Submitted in Partial Fulfillment of the Requirements

for the Degree of Master of Science in Chemistry

Department of Chemistry

FACULTY OF SCIENCE

Chulalongkorn University

Academic Year 2021

Copyright of Chulalongkorn University

การสังเคราะห์นิกเกิลเหล็กเลเยอร์ดับเบิลไฮดรอกไซด์ดัดแปรเพื่อเพิ่มสมบัติทางเคมีไฟฟ้าสำหรับตัวเก็บประจุยิ่งยวด

น.ส.มัชฌิมา มงคลรัตนชัย

Thesis Title	SYNTHESIS OF MODIFIED NICKEL IRON LAYERED DOUBLE HYDROXIDES TO ENHANCE ELECTROCHEMICAL PROPERTIES FOR SUPERCAPACITOR
By	Miss Machima Mongkhonratanachai
Field of Study	Chemistry
Thesis Advisor	Assistant Professor NIPAKA SUKPIROM, Ph.D.
Thesis Co Advisor	Assistant Professor CHAROENKWAN KRAIYA, Ph.D.

Accepted by the FACULTY OF SCIENCE, Chulalongkorn University in Partial Fulfillment of the Requirement for the Master of Science

.... Dean of the FACULTY OF SCIENCE

(Professor POLKIT SANGVANICH, Ph.D.)

THESIS COMMITTEE

.... Chairman

(Professor ORAWON CHAILAPAKUL, Ph.D.)

.... Thesis Advisor

(Assistant Professor NIPAKA SUKPIROM, Ph.D.)

.... Thesis Co-Advisor

(Assistant Professor CHAROENKWAN KRAIYA, Ph.D.)

.... Examiner

(Assistant Professor NUMPON INSIN, Ph.D.)

.... External Examiner

(Assistant Professor Jinda Yeyongchaiwat, Ph.D.)

มัชฌิมา มงคลรัตนชัย : การสังเคราะห์นิกเกิลเหล็กเลเยอร์ดับเบิลไฮดรอกไซด์ดัดแปร
เพื่อเพิ่มสมบัติทางเคมีไฟฟ้าสำหรับตัวเก็บประจุยิ่งยวด. (SYNTHESIS OF MODIFIED
NICKEL IRON LAYERED DOUBLE HYDROXIDES TO ENHANCE
ELECTROCHEMICAL PROPERTIES FOR SUPERCAPACITOR) อ.ที่ปรึกษาหลัก : ผศ.
ดร.นิปกา สุขภิรมย์, อ.ที่ปรึกษาร่วม : ผศ. ดร.เจริญขวัญ ไกรยา

งานวิจัยนี้มุ่งเน้นสังเคราะห์ NiFe LDH ที่ถูกปรับปรุงด้วย Mn เพื่อลดความต้านทาน ซึ่ง
ส่งผลให้ความสามารถในการเก็บพลังงานเพิ่มขึ้นได้ โดยการเตรียมด้วยวิธีการตกตะกอนร่วมที่
50 องศาเซลเซียสเป็นเวลา 6 ชั่วโมง และตรวจสอบโครงสร้างด้วยเทคนิค ICP, XRD, SEM-
EDX และ FTIR จากนั้นทดสอบทางไฟฟ้าเคมีด้วยวิธี CV และ GCD เพื่อหาความสามารถในการ
เก็บประจุ ความต้านทานของสารตัวอย่างถูกวัดด้วยความสัมพันธ์ระหว่างกระแส และความต่าง
ศักย์ และ การศึกษาอิมพีแดนซ์สเปกโตรสโคปีเชิงเคมีไฟฟ้า (EIS) พบว่าการปรับปรุงด้วยแมงกานีส
ส่งผลต่อความสามารถในการเก็บประจุ โดยเมื่อทดสอบด้วยวิธี CV พบว่า NiFeMn LDH
3: 2: 0.98 และ 3: 2: 1.7 เก็บประจุได้เพิ่มขึ้น 2 เท่า เมื่อเทียบกับ NiFe LDH ก่อนปรับปรุง
(จาก 24.72 F/g เป็น 48.58 F/g และ 45.86F/g) นอกจากนี้ วิธี GCD แสดงให้เห็นว่า
ความสามารถในการเก็บประจุเพิ่มขึ้นจาก 89.32 F/g เป็น 203.3 F/g และ 207.6 F/g ตามลำดับ
ค่าความต้านทานโอห์มของ LDH ที่ถูกปรับปรุง ต่ำกว่า NiFe LDH 4.5 เท่า และยังพบว่า NiFeMn
LDH 3: 1: 1.7 ไม่มีความต้านทานการจากกระบวนการส่งผ่านอิเล็กตรอนอีกด้วย แสดงให้เห็นว่า
การปรับปรุงด้วย Mn สามารถเพิ่มความสามารถในการเก็บประจุได้จริงจากการลดความต้านทาน
ของ LDH

สาขาวิชา	เคมี	ลายมือชื่อนิสิต ....
ปีการศึกษา	2564	ลายมือชื่อ อ.ที่ปรึกษาหลัก ....
		ลายมือชื่อ อ.ที่ปรึกษาร่วม ....

6270204123 : MAJOR CHEMISTRY

KEYWORD:

Machima Mongkhonratanachai : SYNTHESIS OF MODIFIED NICKEL IRON LAYERED DOUBLE HYDROXIDES TO ENHANCE ELECTROCHEMICAL PROPERTIES FOR SUPERCAPACITOR. Advisor: Asst. Prof. NIPAKA SUKPIROM, Ph.D. Co-advisor: Asst. Prof. CHAROENKWAN KRAIYA, Ph.D.

This research aimed to synthesize Mn-doped NiFe LDHs in order to decrease resistivity, which can result in an increase in specific capacity. Mn-doped NiFe LDHs were synthesized using simple coprecipitation method at 50 $^{\circ}$C for 6 hours. Their characteristics were confirmed by ICP, XRD, SEM-EDX and FTIR. Electrochemical measurements such as CV and GCD were employed to evaluate their specific capacities. Current voltage relationship and EIS were used to analyse electrochemical properties and resistivities. Through the doping manganese, the specific capacity could be altered. Investigated by CV, the specific capacity of Ni: Fe: Mn 3: 2: 0.98 and 3: 2: 1.7 possessed the electrical capacities of 48.58 F/g and 45.86 F/g that were a 2-fold increase as compared to the 24.72 F/g of NiFe LDH. Similar to the trend found from CV, the specific capacities obtained from GCD increased from 89.32 F/g of NiFe LDH to 203.3 F/g and 207.6 F/g of Ni: Fe: Mn 3: 2: 0.98 and 3: 2: 1.7, respectively. The higher capacity of Mn-doped LDHs might relate to the lower ohmic resistivity. The ohmic resistivity of doped LDH was approximately 4.5 times lower than that of NiFe LDH. The charge transfer resistance of NiFeMn LDH 3: 2: 1.7 was undetected. This work can demonstrate that doping with Mn can increase specific capacity from the decrease of resistance in LDH.

Field of Study:	Chemistry	Student's Signature	....
Academic Year:	2021	Advisor's Signature	....
		Co-advisor's Signature	....

ACKNOWLEDGEMENTS

TABLE OF CONTENTS

LIST OF TABLES

จุฬาลงกรณ์มหาวิทยาลัย

CHULALONGKORN UNIVERSITY

LIST OF FIGURES

Page

LIST OF ABBREVIATIONS

A	ampere
A	area of CV peak
AC	alternating current
A_g	area under graph
ASC	asymmetric supercapacitor
ATR	attenuated total reflectance
C	capacity
CNTs	carbon nanotubes
C_p	specific capacity
CV	cyclic voltammetry
d	d spacing
EDLC	electrical double layer capacitance
EIS	electrochemical impedance spectroscopy
ESR	equivalent series resistance
FTIR	Fourier transform infrared spectrophotometer
GCD	galvanostatic charge discharge
Hz	hertz
I	current
ICP	Inductively coupled plasma
JCPDS	power diffraction standards
k	scan rate
LDH	layered double hydroxide
NF	nickel foam
Q	charge
rGO	reduced graphene oxide

R_{ct}	charge transfer resistance
R_s	ohmic resistance
SEM-EDX	Scanning electron microscopy – energy dispersive x-ray spectroscopy
XRD	X-ray diffractometer
Z	impedance modulus
ZIF-8	zeolite imidazolate frameworks-8
θ	diffraction angle
λ	wavelength

CHAPTER 1 INTRODUCTION

Statement of the problems

Energy is obviously one of the most important factors in human society; therefore, the development of energy system is constantly needed. Supercapacitor is one of the energy storage systems that provides quick surge of energy due to its high power density and long life cycle. The storage mechanism of the first-generation supercapacitor is based on electrical double layer capacitance (EDLC). EDLC performance is limited by a surface, causing a confined physical storage and hence low specific capacity. This leads to the discovery of pseudocapacitor that relies on the reversible faradaic charge transfer (redox reaction) to enhance energy density and specific capacity. The compounds of transition metals, such as Co, Fe, Mn, and Ni, are normally used in pseudocapacitors [1-6].

One of the up-and-coming candidates is layered double hydroxides (LDH) due to their high surface area, stability in ambient atmosphere, and alkaline resistivity. LDH possesses a brucite-layered structure in which several types of metals fill in the octahedral holes of hydroxide ions. The general formula of LDH is $[M^{II}_{1-x}M^{III}_x(OH)_2]^{x+}$ $[A^{n-}_{x/n}mH_2O]$, where M^{II} and M^{III} are metal ions with the oxidation states of 2+ and 3+, and A^{n-} is an interlayer ion which is used to stabilize LDH structure. The ability to substitute various types of metal ions without changing a crystal structure allows the possibility of LDH to have high redox activity, which is a key role in the materials used for pseudocapacitor. The storage mechanism of LDH is a reversible change of the oxidation states of transition metals, $M^{II}(OH)_2 + OH^- \leftrightarrows M^{III}OOH + H_2O + e^-$ [7]. In recent years, a few couples of M^{II}/M^{III} in LDHs have been investigated for their application in supercapacitors [7]. CoFe LDH showed a specific capacitance as high as 2358.4 F/g at 0.5 A/g [8], but cobalt is hazardous. More environmental-friendly choice, NiMn LDH showed a specific capacitance of 1511 F/g at 2.5 A/g [9]; however,

it suffered from low electrical conductivity. The charge transfer resistance of non-binder electrode NiMn LDH was at least 4.1 Ω [9] while that of NiFe LDH was non-detectable by electrochemical impedance spectroscopy (EIS) method [10]. Moreover, the capacitance of NiFe LDH was reported to be 2708 F/g at 5 A/g [10]. It could be noticed that the low specific capacity of LDH is related to its low electrical conductivity of LDH; therefore, the poor conductivity hinders its potential application as a supercapacitor. On the other hand, CoMn LDH [11] has higher specific capacitor compared to CoFe LDH [12], leading us to focus on using manganese as a doping materials in this work.

There are numerous ways to increase the capacity, such as growing LDH on conductive materials, changing metal couples, controlling morphology, or doping LDH with other transition metals. Several reports have been published on the potential of three element LDH [13-15]. The doping of manganese into NiCo LDH increased its specific capacity due to multiple oxidation states of manganese that could enhance the redox activity [15].

In this work, we aimed to improve the electrochemical and electrical properties of NiFe LDH by doping manganese into its structure in order to introduce the possible multiple oxidation states of Mn that could lead to higher specific capacity.

Objectives

1. To synthesize Mn-doped NiFe LDH by co-precipitation method

2. To evaluate the electrochemical and electrical properties of Mn-doped NiFe LDH

Scope of thesis

1. Mn-doped NiFeLDH with various ratios of Ni: Fe: Mn (3: 2: 0.98 and 3: 2: 1.7) and the undoped NiFe LDH and NiMn LDH were synthesized.

2. The prepared LDHs were characterized by ICP, XRD, SEM-EDX, and FTIR.

3. Electrochemical performances were studied by cyclic voltammetry, galvanostatic charge discharge, and cycling performance.

4. The electrical conductivities were investigated by either current-voltage relationship analysis or electrochemical impedance spectroscopy.

จุฬาลงกรณ์มหาวิทยาลัย
CHULALONGKORN UNIVERSITY

CHAPTER 2 LITERATURE REVIEW

2.1 Energy storage

Energy storage is an electrical energy capture device from the energy source. Various types of energy producers are unable to store energy, such as solar cells and wind power, so they cannot produce the energy in overcast sky or wind dropped day. Energy storage is used to trap energy over a period of time for later use. This plays a key role in energy grid [16] because energy storage provides energy as required. Rechargeable energy storage is the most popular in this century because people are concerning about global warming around the world [17]. There are two fundamental ways to store energy [18]. First is the direst way that negative and positive charges are stored on electrode plates. This is called a non faradic process. Another is a faradic process in which electrical energy is changed to chemical energy via the change of oxidation states in cathode. Also, electricity in anode can be stored through the mechanisms such as ion intercalation (as in lithium battery) and pseudo capacitive behavior (as in supercapacitors) [19].

2.2 Capacitor

Capacitor is the electronic device that can store energy in an electrical field. Capacitor has two parallel conductive plates which are separated by dielectric materials. Because the dielectric material is an insulator, the system seems like an open circuit. Electrons from a power source were stuck on a negative site while they were attracted by positive charges on another plate. The capacity of capacitor is ranged by surface area, dielectric constant, and inverse to the distance between conductive plates as shown in equation 2.2.1.

$$C = \varepsilon_r \frac{A}{d} \qquad\qquad 2.2.1$$

C = capacity (F)

ε_r = dielectric relative permittivity constant (F/m)

A = area of parallel plate (m^2)

d = distance between parallel plate (m)

The ideal capacitor would have high power density and fast charge discharge properties. This advantage allows its application as a starter in an electronic device such as an electric fan [20]. Moreover, a capacitor can also compensate for power factor lag or phase shift in alternating current (AC) power supplies [21].

2.3 Supercapacitor

The difference between capacitor and supercapacitor is the way to collect charges. Capacitor stores the charge on each side of metal sheets. Dielectric insulator is placed in the middle of two metallic sheets. On the other hand, a supercapacitor can store more energy than a capacitor because there is the difference in charge mechanism. There are three types of supercapacitors: electrochemical double layer (EDLC), pseudo capacitor, and hybrid-capacitor.

The first generation supercapacitor, EDLC, uses materials with high surface area such as activated carbon. While charging occurs, electrolyte stabilizes the charge as shown in figure 2.1(a) [22]. Here, it looks like each electrode acts as an individual capacitor. The amount of stored energy depends on surface area and electrostatic interaction.

Pseudocapacitor has been developed to increase specific capacity, based on a faradaic process (figure 2.1(b)). Energy is stored as chemical energy via redox reaction of metal transitions, such as RuO_2, MnO_2 [23] and Fe_3O_4, making the

pseudocapacitor system more stable than EDLC. The example of such redox reaction is shown here,

$$RuO_2 + xH^+ + xe^- \rightleftharpoons RuO_{2-x}(OH)_x \text{ [24]}.$$
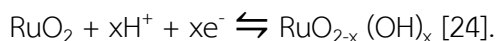
Hybrid capacitor is a device that combines EDLC and pseudocapacitor (figure2.1(c)). Hybrid supercapacitor can fix the problems of unstable charge collection and charge limitation of EDLC using the advantage of a pseudocapacitive part. The capacity increases because there is no surface area limit. On the other hand, the part of EDLC has no problem in the collapse of metal transition structures that could happen in a pseudocapacitive part. Because some redox reactions are quasi reversible reaction, the oxidation state of metal transitions, which have changed, cannot completely go back to the original state.
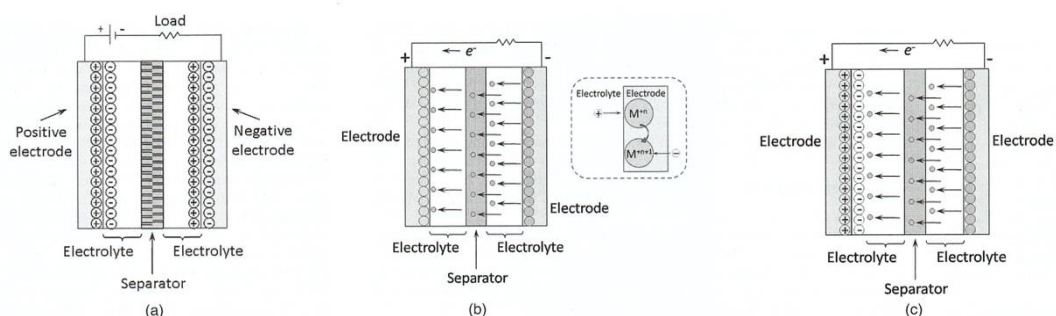
Figure 2.1 The storage mechanisms of a) EDCL, b) pseudocapacitor, and c) hybrid capacitor [22]

2.4 Asymmetric supercapacitor (ASC)

There is no clarified definition between asymmetric supercapacitor and hybrid capacitor. In several research studies, hybrid capacitors are referred to ASC [24]. In some instances, battery like electrodes (intercalation type) are also called ASC [23]. Yuanlong Shao et al. made an argument that hybrid capacitors are a subset of ASC. The group commented that the main characteristics of ASC is a difference in electrode materials in cathode and anode, even if the storage mechanism of both electrodes is the same [25]. High specific capacity of ASC is related to reversible

faradic process [24], thin dielectric layer [26], high surface area and high conductivity [27]. LDH has been reported as a cathode in ASC with activated carbon as an anode [1-7, 9-13, 28].

2.5 Layered double hydroxides (LDH)

LDH is the synthetic clay materials constituted by the brucite layers of the octahedral units of metal hydroxides as shown in figure 2.2.
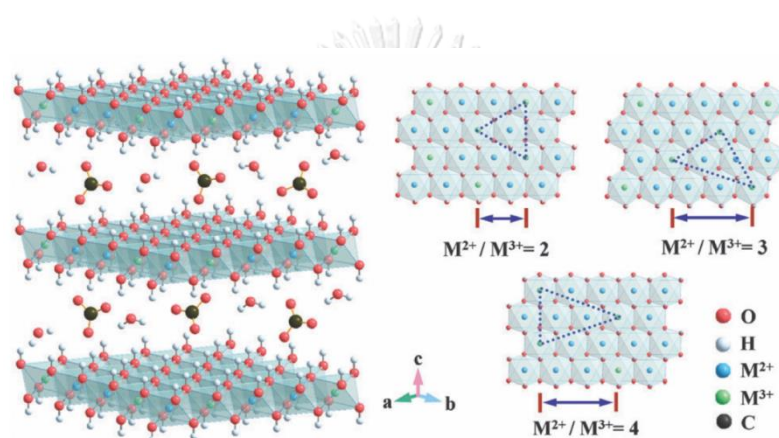
Figure 2.2 The idealized structure of LDH with different ratios of M^{II}/M^{III} [29]

The general formula of LDH is $[M^{II}_{1-x}M^{III}_x(OH)_2]^{x+}[A^{n-}_{x/n}mH_2O]$, where M^{II} and M^{III} are metals with the oxidation states of 2+ and 3+, and A^{n-} is an interlayer ion. The LDH structure could accommodate wide types of di- and tri-valence cations [1-6] and various ratios of M^{2+}: M^{3+} [30, 31]. The M^{2+}: M^{3+} ratios such as 1: 1, 1: 2, 1: 4, 3: 1 and 3: 2 are commonly reported. LDH morphology [30] and the d-spacing of LDH [31] are influenced by M^{2+}: M^{3+} ratio (table 2.1). The shape of NiCo LDH, for example, could change from nanosheets of 1: 1 LDH to nanospheres of 1: 2 LDH then to nanorods of 1: 4 LDH. As indicated in table 2.1, increasing the Ni ratio in NiCo LDH lowered the d spacing (101) [31].

Table 2.1 The d-spacing of (101) lattice plane with different Co: Ni ratio

Composition	2 theta (101)	$d_{(101)}$ XRD (nm)	$d_{(101)}$ HRTEM (nm)
$Co_{0.2}Ni_{0.8}(OH)_2$	38.42	2.340202	2.34
$Co_{0.5}Ni_{0.5}(OH)_2$	38.17	2.354953	2.36
$Co_{0.8}Ni_{0.2}(OH)_2$	37.92	2.369902	2.38

Hydrothermal method, reflux, coprecipitation, electrodeposition and solvothermal method can all be used to synthesize LDH. LDH has the potential to be used in a wide range of applications, including oxygen evolution catalysts [32, 33], photocatalysts, flame retardants, sensors, drug deliveries, adsorbents, cosmetics, and energy storages [34]. These variety of applications takes advantage of LDH that offers distinct properties such as large surface area [35], environmental friendly [36], stability in the ambient atmosphere, alkaline resistivity, high redox activity [15] and the ability to interchange metal centers without altering the crystal structure [7].

2.6 LDH as a supercapacitor

Previous reports have shown that LDH could act as a supercapacitor. Its charge-discharge mechanism is $Ni^{II}(OH)_2 + OH^- \leftrightarrows Ni^{III}OOH + H_2O + e^-$ [7]. The OH^- in an electrolyte plays a key role in storage mechanism. There are various ways to increase capacity of LDH such as adding conductive materials [1, 4, 37-40], changing the types of metals in M(II)/M(III) couple [1-6, 37] , controlling morphology [31, 41, 42], and doping other metals [13-15, 35].

Many kinds of conductive materials such as ZIF-8 [1], graphene oxide [4], carbon cloth [37], carbon nanotube [38], MnOOH [39] and reduced graphene oxide aerogel (rGO aerogel) [40] were added during the synthesis of LDH in order to enhance ionic and electronic mobilities. The ohmic resistance of NiAl LDH was reduced by ZIF-8 from 1.69 to 1.08 Ω while the charge transfer resistance was

reduced from 1.8 to 0.85 Ω. As compared to NiAl LDH, ZIF-8@NiAl LDH had greater ion diffusion [1]. The rGO aerogel decreased charge transfer resistance of NiFe LDH from 8.7 Ω to 5.5 Ω meanwhile the specific capacity increased [40].

Many types of LDH such as NiAl [1-3], NiCo [4], NiFe [5], NiMn [6], CoFe [12] and CoMn [11] have been studied as materials for supercapacitors. Nickel-based LDH has attracted a lot of attention since Ni is ecologically safe, high electrically conductive, and inexpensive [36]. Table 2.2 shows the specific capacities of Ni-based LDHs. From this review, the specific capacity is based not only on the type of LDH but also on the synthesis method, conductive materials and supporting electrodes.

Table 2.2 The specific capacity of LDH

Electrode materials	Specific capacity(F/g)	Current density
Reflux NiAl LDH [1]	106	1 A/g
NiAl LDH grown on MWCNT/NF [2]	938	5 mA/cm^2
Hollow microspheres NiAl LDH [3]	1578	1 A/g
NiCo LDH@rGO [4]	1703	0.5 A/g
Spherical NiFe LDH [5]	168	1.5 A/g
NiFe growth on NF [10]	2708	5 A/g
NiMn LDH nanosheet synthesized by reverse micelle method [6]	881	0.5 A/g
NiMn growth on NF [9]	1511	2.5 A/g

Morphology of LDH is another important factor due to it relates to the packing of active materials on current collector and electroactive sites [10]. Ultrathin nanosheet which had 14 nm thickness showed higher specific capacity of 2708 F/g as compared to the one with 56 nm thickness (1456 F/g) [10]. Moreover, the Ni: Co ratio

was controlled with the purpose of changing the morphology [30]. The nanospheres with a Ni: Co ratio of 1: 2 had the highest specific capacity of 1147 F/g. The nanosheets with a 1: 1 Co: Ni ratio, on the other hand, had the lowest specific capacitor of 754 F/g.

2.7 Metal-doped LDH

With the goal of improving electrochemical performance, several forms of metal doping LDH were examined. In prior studies, Cobalt was doped into NiMn LDH. [13, 14]. The studies observed the increase in capacitance of Co-doped NiMn LDH as compared to pristine LDH. 10% Co-doped NiMn LDH possessed 1148 F/g at 1 A/g, which was nearly twice to the undoped NiMn LDH [13]. Mg-doped CoAl LDH also showed higher capacity and stability than its undoped counterpart [35]. MgCoAl LDH displayed 451.7 F/g which was over 3 times higher than CoAl LDH. MgCoAl LDH cycling performance was 97.6% while MgAl LDH was 95.4% after the 18th cycle. NiCoAl LDH showed higher specific capacity (960 F/g) than NiAl LDH (140 F/g) and CoAl LDH (approximately 420 F/g) [43]. Ce, which has high electrical conductivity, was doped in NiCo LDH-CNTs. The result could reduce a resistance from 39.4 to 9.4 Ω and led to the increase in specific capacity from 43.5 to 106.6 F/g.

2.8 Mn-doped LDH

Manganese has many oxidation states, from 2+ to 7+. The oxidation state plays a key factor in the storage mechanism [15] because supercapacitor stores energy by changing the oxidation state of transition metals. According to the literature reviews, CoMn LDH (1079 F/g) [11] had a greater specific capacity than CoFe LDH (774 F/g) [12], while Mn-doped NiCo LDH had 4-fold increase in the capacity as compared to the original one [15]. These literature reviews suggest that doping Mn

could increase the specific capacity of LDH. Moreover, NiFeMn has been successfully synthesized and reported as a catalyst for water oxidation reaction [33].

2.9 Coprecipitation

The coprecipitate method is a simple technique that occurs in mild conditions and ambient temperature, giving a cost effective product. There are two steps during precipitation: nucleation and growth, which are key factors in controlling a particle size. In this process, the rate of nucleation and growth is controlled by pH [36, 44]. Normally, high pH is suitable for precipitating metal salts. The desired products are prepared from the starting precursors of metal salts with stoichiometric ratio. Metal salts, such as metal nitrates or metal chlorides, are commonly used as precursors [45]. Sodium hydroxide, urea, and ammonia are used as alkali solutions.

2.10 Inductively coupled plasma-optical emission spectrometry (ICP-OES)

In this work, the exact ratio of each metal in LDH was determined using ICP-OES. LDH samples were completely dissolved in acid, and the concentration of each metal was calculated using the standard calibration curve of each metal.

The schematic of ICP-OES is shown in figure 2.3. ICP-OES is a quantitative technique in which the plasma of argon gas atomizes the sample as well as excites the inner electrons. When the electrons return to their ground states, the characteristic emission spectra of individual types of atoms are observed. The plasma at a temperature of 700 K is induced via electromagnetic induction at 27 MHz and the radio frequency of 1-5 kV. ICP-OES is commonly used at selected wavelengths that fit to the spectra of specific elements in the sample. The intensity of emission spectrum is proportional to the amount of that specific element in a sample.
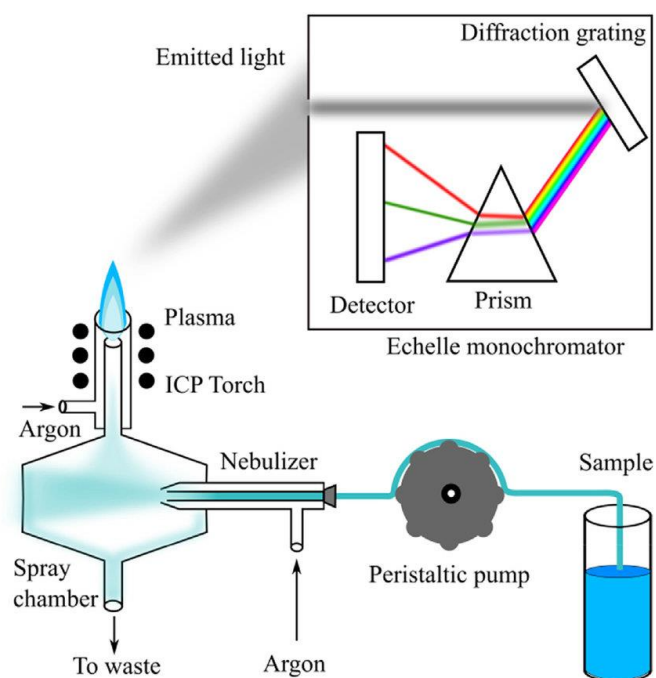
Figure 2.3 The schematic of ICP [46]

2.11 X-ray diffraction (XRD)

In this work, XRD was used to identify the crystalline phase of the synthesized LDH. The XRD plots of the scatter angles and intensities show the peak patterns that are a fingerprint of each material. The pattern was then compared to the Joint Committee on Powder Diffraction Standards (JCPDS).

XRD is a nondestructive method for the determination of a crystal structure and the phase identification of solids. The technique normally uses the X-ray of Cu K_α. The beam of X-ray hits the samples, and the scattered rays are sent to a detector as shown in figure 2.4. The diffraction peak appears according to Bragg's law (equation 2.11.1).
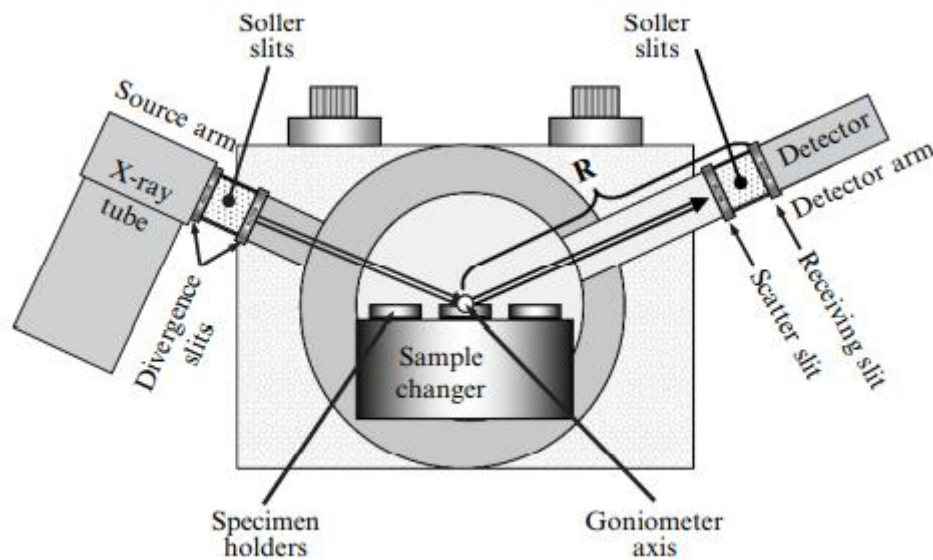
Figure 2.4 The schematic of X-ray diffraction [47]

$$n\lambda = 2d\sin\theta \qquad\qquad 2.11.1$$

n = integer number

λ = x-ray wavelength (nm)

d = d spacing (distance between the plane) (nm)

θ = diffraction angle (degree)

2.12 Scanning electron microscopy-energy dispersive x-ray spectroscopy (SEM-EDX)

SEM was used to examine the morphology and size of LDH while EDX was used to monitor the metal distribution in LDH.

Figure 2.5 shows the schematic of SEM. Electron beam with high energy from tungsten filament is focused by magnetic lens. The surface of a sample reflects the focused beam and emits secondary electrons and characteristic X-rays. The secondary electron is detected, and the voltage of the electron displays the

morphology of the sample in two dimensions. By detecting X-rays, energy dispersive X-ray analysis is used to analyze the types and amounts of each element on the surface of a sample. When inner electron is kicked off by an electron beam, the electrons at the following level descend and emit distinctive X-rays that are unique to each element.
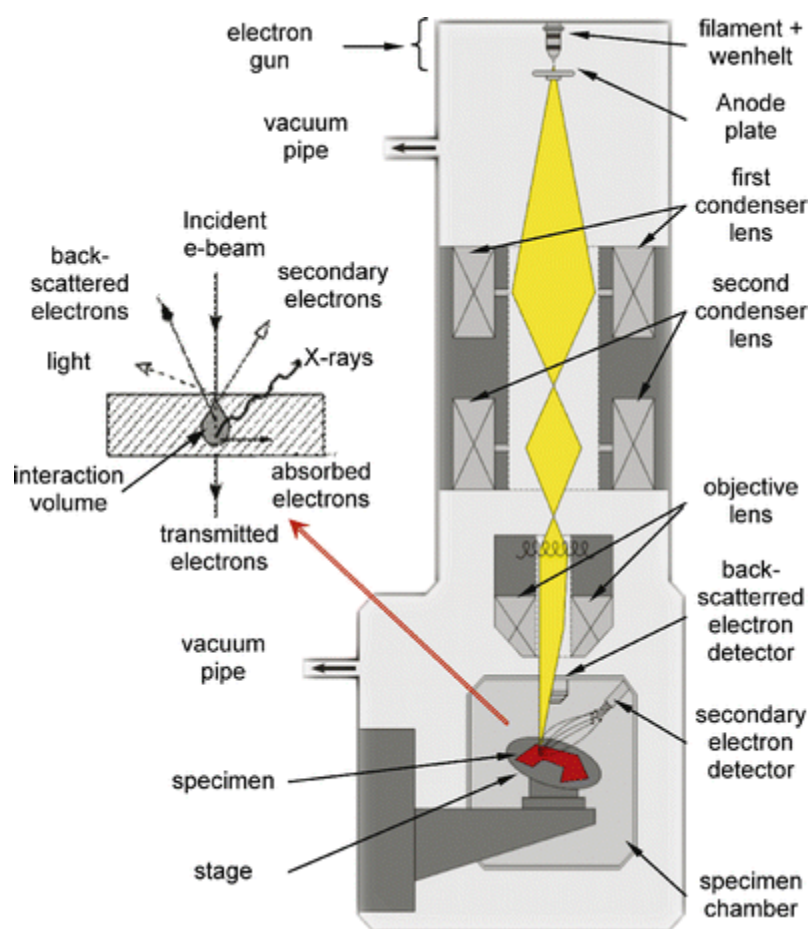
Figure 2.5 The principle of scanning electron microscope (SEM) column and image processing [48]

2.13 Fourier transform infrared spectrophotometry (FTIR)

FTIR was used to confirm the existence of specific functional groups in LDH. The appearances of OH vibration from double hydroxide and inter layer water and

CO_3^{2-} vibration from the interlayer anions were expected. The nondestructive method, Attenuated Total Reflectance (ATR), was used in this work.

There are two general modes to detect the wavelengths of IR absorption: the transmission mode of KBr pellet and the ATR mode of pure sample. ATR is a nondestructive method using IR beam to probe a sample through the ATR crystal at the angle greater than its critical angle. The beam reflects back on crystal and its intensity gets detected as shown in figure 2.6.
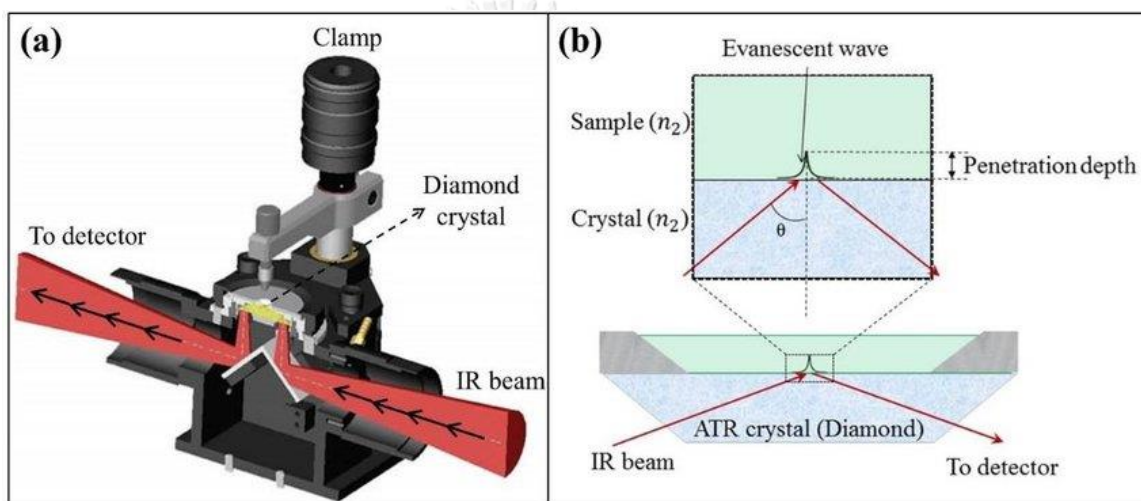
Figure 2.6 The schematic of ATR-FTIR at the interface of crystal [49]

Percentage transmittance indicates the region where sample absorbs the energy as it vibrates. Bonds can move in three different ways: symmetric stretching, asymmetric stretching, and bending (figure 2.7). The energy matched to bond motivation is absorbed. This can identify chemical functional groups.
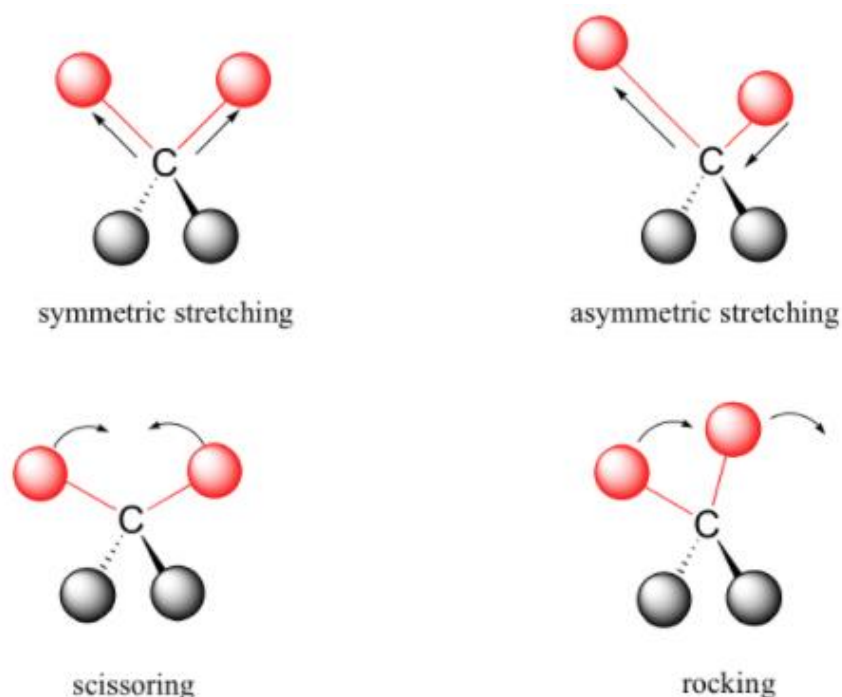
Figure 2.7 IR active vibration modes [50]

2.14 Cyclic voltammetry (CV)

Cyclic voltammetry is the technique that generates cycles of voltage and collects the corresponding current. The prompt change in current refers to the change in metal oxidation state via redox reaction as shown in figure 2.8. CV can also show the charging type of electrode as shown in figure 2.9 [51]. EDCL materials, which store electrons on carbon surface, show rectangular curve while pseudocapacitive materials show redox peaks.

The CV system requires three electrodes: a working electrode, a reference electrode and a counter electrode. Sample pieces could be used as working electrode. Reference electrode such as Ag/AgCl is used to refer to the working electrode voltage. Platinum (Pt) is commonly used as the counter electrode since it is inert and does not react with other materials in many systems.
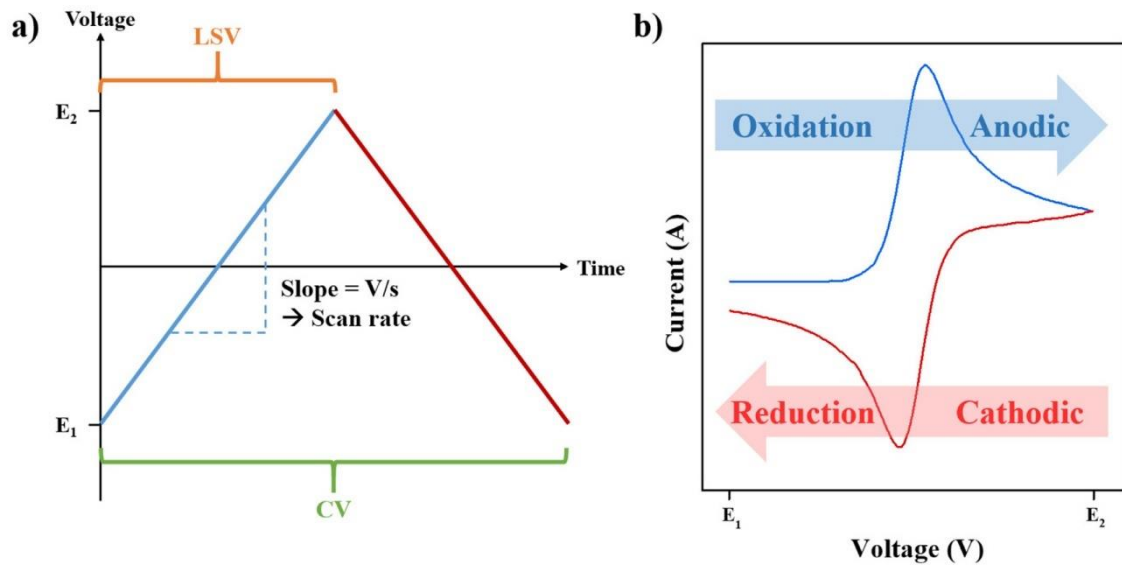
Figure 2.8 The schematic of cyclic voltammetry (a) relationship between voltage and time and (b) cyclic voltammetry plot [52].
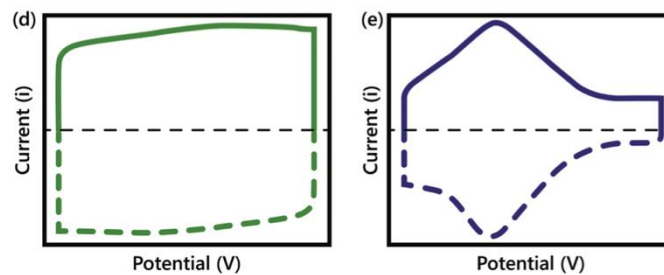
Figure 2.9 The cyclic voltammograms of a) EDCL and b) pseudocapacitive [51]

Here, the area of CV curves was used to estimate a capacity. The following equations (2.14.1-2.14.7) explain the relationship between the CV area and a capacity.

$$C = \frac{Q}{V} \qquad\qquad 2.14.1$$

When Q is charge in coulombs, and V is voltage studied [53].

Specific capacity (C_p) is derived as shown below when m is the mass of active material.

$$C_p = \frac{Q}{mV} \qquad\qquad 2.14.2$$

$$Q = It \qquad\qquad 2.14.3$$

Place 2.14.3 in 2.14.2.

$$C_p = \frac{It}{mV} \qquad\qquad 2.14.4$$

Where V/t = scan rate = k

$$I = C_p mk \qquad\qquad 2.14.5$$

Area under graph (A_g) is calculated by integration of current by dV.

$$A_g = \int_{V_1}^{V_2} IdV$$

This equation shows the same as integral of eq 2.14.5 by dV.

$$A_g = \int_{V_1}^{V_2} IdV = \int_{V_1}^{V_2} C_p mk \, dV$$

$$A_g = (V_2 - V_1) C_p mk \qquad\qquad 2.14.6$$

Practically, the area of CV can be obtained by the subtraction of the area under an oxidation curve with that of a reduction curve. When A represents area of CV peak.
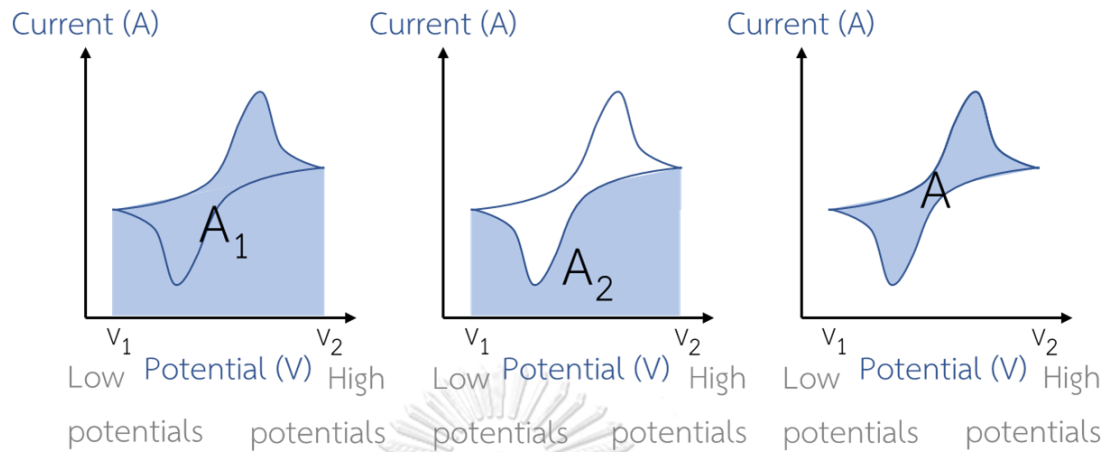
$$A = A_1 - A_2$$

$$A = [(V_2-V_1)C_p mk]-[(V_1-V_2)C_p mk]$$

$$C_p = \frac{A}{2(V_2-V_1)mk}$$

2.14.7

The equation 2.14.7 is generally used to calculate the specific capacity of energy storage materials.

2.15 Galvanostatic charge discharge (GCD)

Inversely to cyclic voltammetry, galvanostatic charge discharge is the method that controls current between a working electrode and a counter electrode while the potential is measured. The result is plotted between potential and time as a charge-discharge curve, figure 2.10. Equivalent series resistance (ESR), which includes all resistances involving with a working electrode such as electrolyte resistance, the transport resistance in porous materials, and the resistance from the external circuit, is calculated by an equation $ESR = \frac{V_{IR\ drop}}{\Delta I}$.
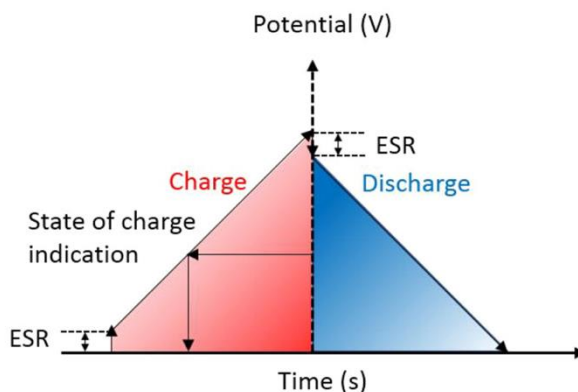
Figure 2.10 The galvanostatic charge discharge behavior of theorical supercapacitor [25]

$$C_p = \frac{It}{m\Delta V}$$ 2.15.1

GCD could be used to evaluate a specific capacity using an equation 2.15.1 [54]. The I/m was current density. Moreover, the cyclability test of GCD showed the performance of electrode after charge-discharge for a large number of cycles.

2.16 Electrochemical impedance spectroscopy (EIS)

This method can characterize electrochemical electrodes. EIS is performed by applying an alternative current (AC) between the working electrode and counter electrode in a narrow sinusoidal voltage range. The frequency is often varied between 10^{-3}-10^{5} Hz, and the corresponding current is measured. Impedance is a frequency-dependent resistance. There are 2 common types of results: Bode and Nyquist plots. The phase angle and impedance modulus (z) can be shown using a Bode plot [51]. The Nyquist plot, which is more recently used, is plotted between real and imaginary impedances. The advantage of Nyquist is that it displays the overall information.

Here, the resistivity of LDH was studied by Nyquist plot as shown in figure 2.11 [55]. The sum of individual frequency independence resistance resulting from electrolyte, current collector and the connection between current collector and active mass was defined as ohmic resistance (R_s) [56]. Charge transfer resistance (R_{ct}) which was shown as a semicircle, demonstrated faradaic reaction on working electrode surface [57]. Warburg impedance from concentration polarization and mass transfer was expressed as a shift from the theoretical 90° [51].
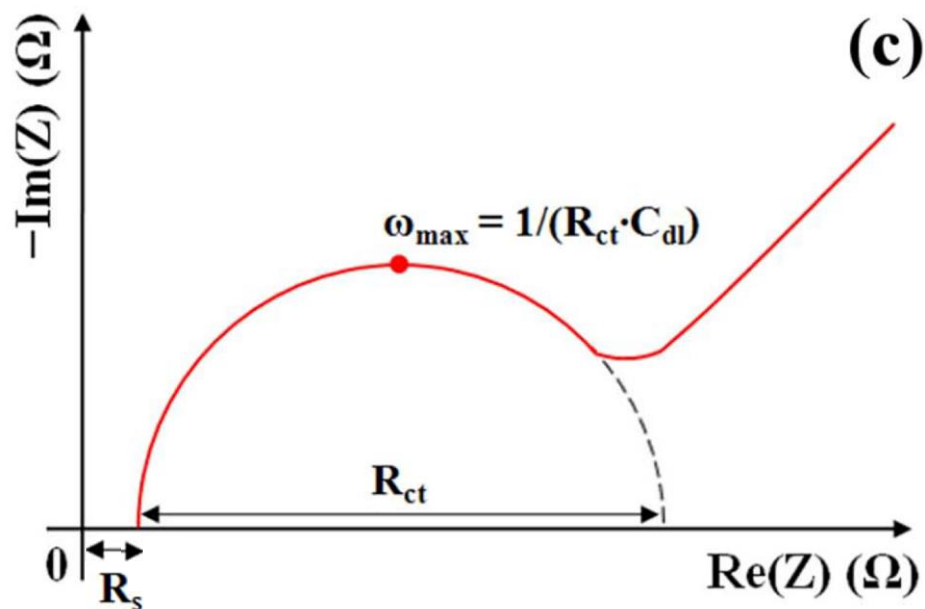
Figure 2.11 Nyquist plot [55]

2.17 Ohm's law

The relationship between voltage (V), current (I) and resistance (R) is shown in the equation 2.17.1.

$$V = IR \qquad\qquad 2.17.1$$

Voltage and current could be measured by a multimeter. The circuit was set up as in figure 2.12.
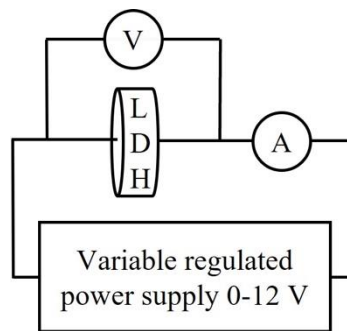
Figure 2.12 Measurement circuit

The current of a sample could be measured in series by an ammeter (A) while the voltage was recorded in a parallel fashion with a voltmeter (V). Resistance, depending on the length and the contact area of material, was normalized to resistivity by equation 2.17.2.

$$\rho = \frac{RA}{l}$$ 2.17.2

ρ = resistivity (Ωm)

R = resistance (Ω)

A = cross section area (m^2)

l = length (m)

CHAPTER 3 EXPERIMENTS

Chemicals

Nickel nitrate hexahydrate (97%, Thermo Fisher Scientific)

Iron nitrate nonahydrate (98%, Thermo Fisher Scientific)

Manganese nitrate tetrahydrate (99.8%, Chem-Supply)

Hydrochloric acid (HCl) (37%, QreC)

Nitric acid (HNO_3) (65%, Supelco)

Sodium hydroxide (NaOH) (99.0%, Merck)

Potassium hydroxide (KOH) (85.0%, Kemaus)

Dimethyl sulfoxide (DMSO) (99.5%, Lab-Scan)

Polyvinylidene fluoride (PVdF) (average Mw~534,000, Sigma Aldrich)

Carbon black (Monarch 800, Carbot)

Ethanal (95%)

Deionize water (DI water)

Equipments

Beaker (150 ml, Duran)

Clamp

Water bath

Magnetic bar

Centrifuge tube (50 ml)

Nickel mesh (Ni mesh) (wire diameter 0.13 mm, Fuelcell Materials)

Agate mortar

Blade

Scotch tape (3M)

Micropipette (1000 μl, Transferpette)

13 mm diameter mold

Copper cage

Pt wire (diameter 2 mm)

silver/silver chloride electrode (Ag/AgCl) (Metrohm)

Multimeter

4-digit balance (SI-234, Denver instrument)

Hotplate and stirrer (C-MAG HS7, IKA)

pH meter (Seven Easy, Mettler Toledo)

Centrifuge

Oven (Memmert)

Ultrasonics (VC505, sonics)

5-digit balance (XR 205SM-DR, Precisa)

Vacuum oven (Eyela)

Instruments

Inductively coupled plasma – optical emission spectrometer (ICP-OES) (iCAP 6500 ICP-OES, Thermo Scientific)

X-ray diffractometer (XRD) (Smartlab 30KV, Rigaku)

Scanning electron microscopy – energy dispersive x-ray spectroscopy (SEM-EDX) (IT-100, JEOL)

Fourier transform infrared spectrophotometer (FTIR) (Nicolet 6700, Thermo Scientific)

Potentiostat (AUT84200 Autolab, Metrohm)

Potentiostat (Pgstat101, Metrohm)

Synthesis of NiFe LDH

Nickel nitrate hexahydrate and iron nitrate nonahydrate were dissolved in DI water in the Ni: Fe ratio of 3: 1. The base solution and the above metal solution were mixed, and the pH of the solution was preserved at 8.5 during the synthesis. The mixture was heated at 50 °C and stirred for 6 hours. After that, DI water and ethanol were used to clean the precipitants. Finally, the product was dried overnight at 60 °C [32]

.

Synthesis of Mn-doped NiFe LDH

NiFeMn LDHs were synthesized similarly to the synthesis of NiFe LDH. Manganese nitrate tetrahydrate was added to the the mixed metal solution of Ni and Fe before mixing with the base solution. The selected two ratios of Ni: Fe: Mn were 3: 1: 0.5 and 3: 1: 1.

Synthesis of NiMn LDH

The method was the same as synthesizing NiFe LDH. Manganese nitrate tetrahydrate was used instead of iron nitrate nonahydrate.

Chemical characterization

The elemental analysis was done with ICP-OES. 10 mg of LDHs was dissolved in 10 drops of aqua regia, and the solution was heated at a mild temperature until only solid was left. Then 1 M nitric acid was added and scaled in a 25 ml volumetric flask. After that, the concentration of LDHs was scaled down 25 times. The concentration of metal was investigated using an external standard method. The crystal structure of the LDHs was characterized by XRD. XRD patterns were recorded with the condition of Cu K$_\alpha$ at 40 kV and 30 mA from 2θ = 5°-80°

with the scan step of 0.01 deg. The scattering slit and receiving slit 1 and 2 were set at 0.5 deg, 5 mm and 5 mm, respectively. The morphology and elemental distribution were examined using SEM-EDX at a voltage of 20.0 kV. The chemical functions of LDH were probed by FTIR in the range of 4000-650 cm^{-1}.

Electrochemical measurements

To remove metal oxide impurities and other surface residues, Ni mesh was cut into $1*2 \ cm^2$ and sonicated in 3 M HCl for 5 min. Then, the mesh was washed with DI water and ethanol 95%, respectively. The cut mesh was dried and weighed. After that, scotch tape was used to cover the upper half of the Ni mesh ($1*1 \ cm^2$) on both sides. The LDH, carbon black, and PVdF in the ratio of 8: 1: 1 were ground to be homogenous powder. The powder was mixed with 150 μl dimethyl sulfoxide (DMSO) to form the slurry. This slurry was cast on the lower half of the nickel mesh as shown in figure 3.1. Then, the electrode was dried overnight in a vacuum at 60 $^{\circ}$C. The LDH weight on the working electrode was in the range of 17.7-21.0 mg. In 3 M KOH, platinum wire and Ag/AgCl were used as a counter electrode and a reference electrode, respectively.
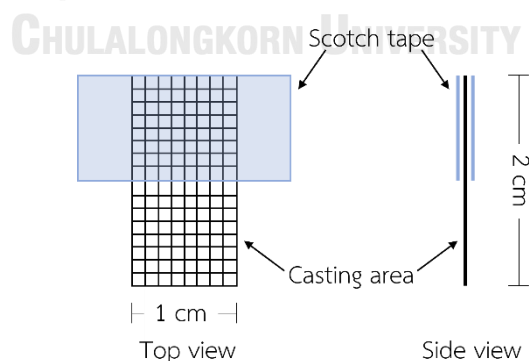

Figure 3.1 The preparation of nickel mesh for casting the electrode materials

Cyclic voltammetry (CV)

CV in 3 M KOH was recorded in the voltage range (ΔV) of -0.1 V to 0.5 V and the scan rate (k) of 0.01 V/s using AUT84200 Autolab potentiostat. The specific capacity (C_p) of the supercapacitor cathodes was calculated from the equation 2.14.7 ($C_p = \dfrac{A}{2(V_2 - V_1)mk}$).

Galvanostatic charge discharge (GCD)

The charging time of electrode was 1000 seconds at the current density of 0.1 A/g using PG101 potentiostatic. Then, the discharged time was collected at -0.1 A/g. The specific capacity (C_p) was calculated from the equation 2.15.1 ($C_p = \dfrac{It}{m\Delta V}$).

Electrical measurement

Current-voltage relationship analysis

The 0.500g of NiFe LDH 3: 1 and NiFeMn LDH 3: 1: 0.5 were pressed uniaxially for 3 minutes at 3 tons in a 13 mm-diameter mold, resulting in a 1.6 mm high cylinder. Silver paint was applied on both sides of the pellet, and the pellet was connected to two copper wires as shown in figure 3.2. Electrical circuit was shown in figure 2.12. The current was recorded at the voltage of 0-12 V. Resistivities were calculated by Ohm's law.
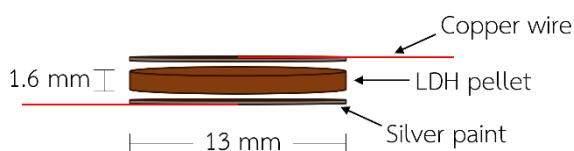
Figure 3.2 LDH pellet

Electrochemical impedance spectroscopy (EIS)

The pellets of samples were prepared in the same way as the study of current-voltage relationship analysis. In order to reduce resistivity, the pressure was increased to 6 tons with 0.2000 g of LDHs to achieve very thin pellets. The EIS of silver covered LDH pellets was recorded in the frequency range of 10,000 Hz to 0.1 Hz with 0.01 V_{RMS} sinus wave amplitude at the internal input connection.

CHAPTER 4 RESULTS AND DISCUSSION

Chemical characterization

Inductively coupled plasma-optical emission spectrometry (ICP-OES)

Table 4.1 showed a real ratio of metals calculated from the amount of each metal obtained from ICP-OES. The R-squared of the Ni, Fe, and Mn calibration curves was 0.999 (appendix figure 6.1). The result ratio showed much less amount of Ni as compared to the expected ratio calculated from the metal precursors. This could be caused by the hygroscopic nature of a nickel precursor. The moist substance reduced the actual number of nickel atoms. From here on, the LDH sample would be reported using the real ratio as NiFe 3: 2, NiFeMn 3: 2: 0.98, NiFeMn 3: 2: 1.7, and NiMn 3: 2 instead of the calculated ratio NiFe 3: 1, NiFeMn 3: 1: 0.5, NiFeMn 3: 1: 1, and NiMn 3: 1.

Table 4.1 The stoichiometry ratio of LDHs from ICP

LDH name		Ni ratio	Fe ratio	Mn ratio
NiFe	3: 2	3.00	1.89	0.01
NiFeMn	3: 2: 0.98	3.00	1.99	0.98
NiFeMn	3: 2: 1.7	3.00	2.04	1.70
NiMn	3: 2	3.00	0.02	2.04

X-ray diffraction (XRD)

Despite the fact that Ni: Fe ratio from ICP did not correspond to the starting weights, the XRD patterns of all samples, shown in figure 4.1, indicated that all of them possessed the LDH structure. This was possible because the layered structure of LDH could accommodate the wild range of metal ratios. XRD patterns of

all synthesized LDHs showed broad peaks at 11°, 22° and 34°, corresponding to (003), (006), and (012) crystal planes (JCPDS: 510463). When the manganese was doped in NiFe LDH, the peak intensities decreased as compared to those of pristine NiFe LDH. Lower intensity after doping Mn was predicted due to the structure distortion resulting from Mn replacement on metal lattice sites in the structure of NiFe LDH [58]. Without any impurity peak of other metal oxides, this indicated that Mn was successfully doped into the octahedral holes of hydroxide ions without affecting the crystal system.
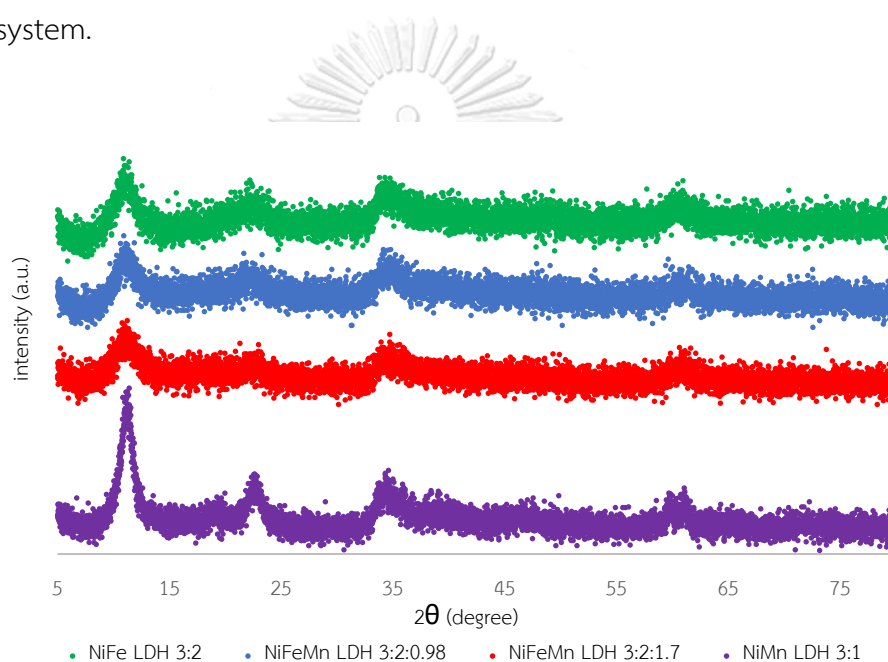
Figure 4.1 The XRD patterns of NiFe LDH, NiFeMn LDH 3: 2: 0.98, NiFeMn LDH 3: 2: 1.7, and NiMn LDH

Scanning electron microscopy-energy dispersive x-ray spectroscopy (SEM-EDX)

The stacking of the LDH layers was clearly seen in SEM images (figure 4.2) that could confirm the basic structure of layered materials. The synthesized LDH was found in a variety of sizes, ranging from 50 to 100 micrometers. The wide size distribution was common when the synthesis method was a quick coprecipitation.

Figure 4.2 SEM images at x100, x250, and x500 (a) NiFe LDH, (b) NiFeMn LDH
3: 2: 0.98, (c) NiFeMn LDH 3: 2: 1.7, and (d) NiMn LDH

The homogeneous distributions of nickel, iron and manganese over all LDH particles were validated by EDX mapping (figure 4.3). The well distribution of these metals over every particle could be another evidence that the impurities in synthesized LDH was not detected.
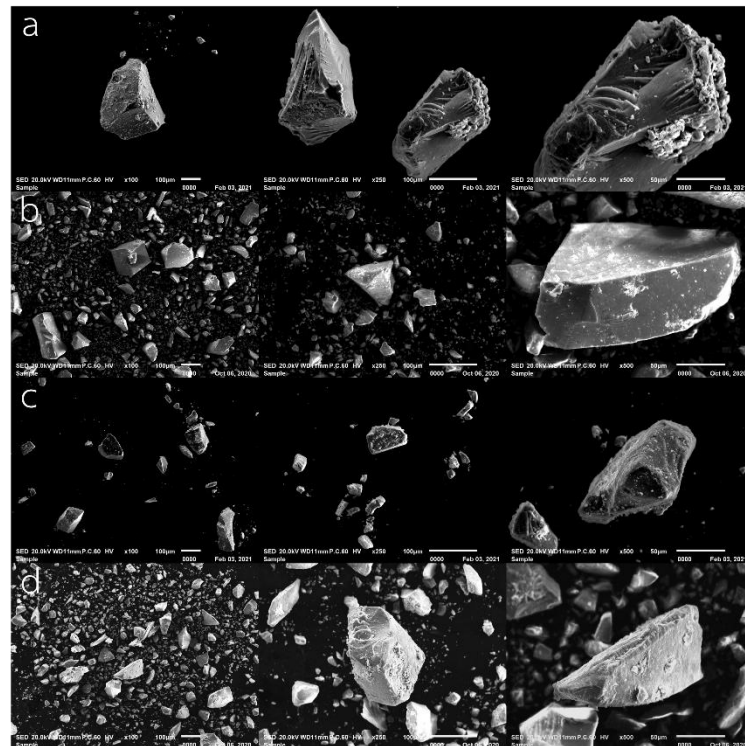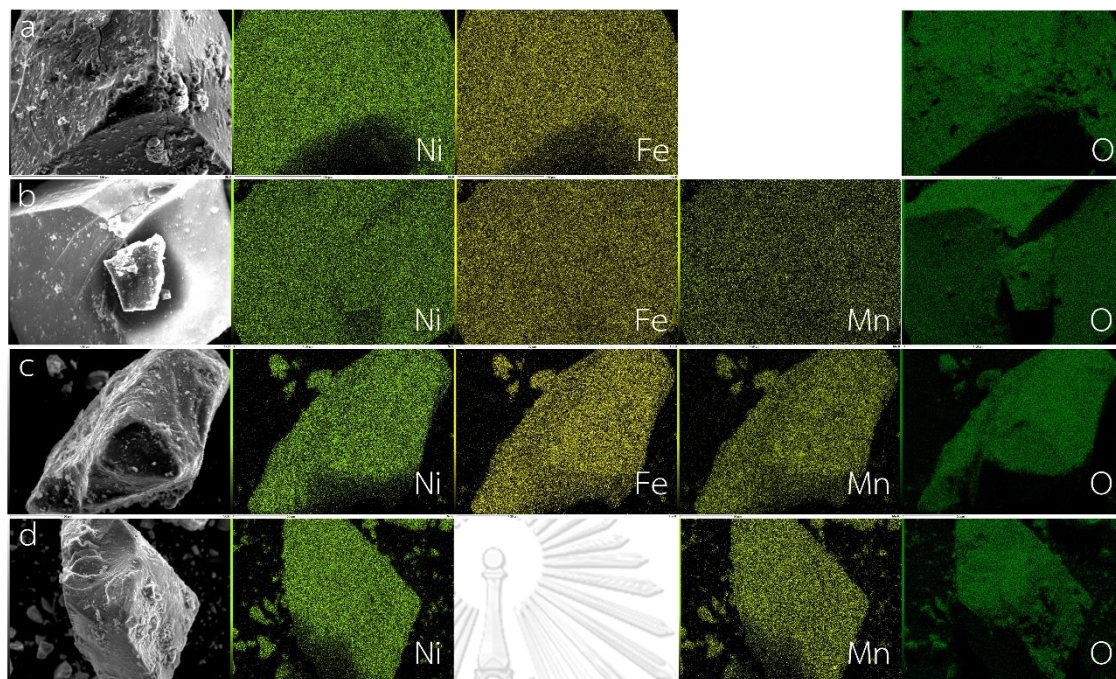
Figure 4.3 The EDX images of (a) NiFe LDH, (b) NiFeMn LDH 3: 2: 0.98, (c) NiFeMn LDH 3: 2: 1.7, and (d) NiMn LDH showing the distribution of nickel, iron, manganese, and oxygen

Fourier transform infrared spectrophotometry (FTIR)

FTIR absorption spectra (figure 4.4) confirmed the presence of three common functional groups found in LDH. A strong and broad peak at ca. 3373 cm^{-1} and a medium sharp peak at 1634 cm^{-1} were attributed to OH stretching and OH bending, respectively, of hydroxide and interlayer water. The interlayer carbonate anion, normally found in the interlayers of LDH due to the dissolution of CO_2 in aqueous solution, was assigned at 1343 cm^{-1} [10].
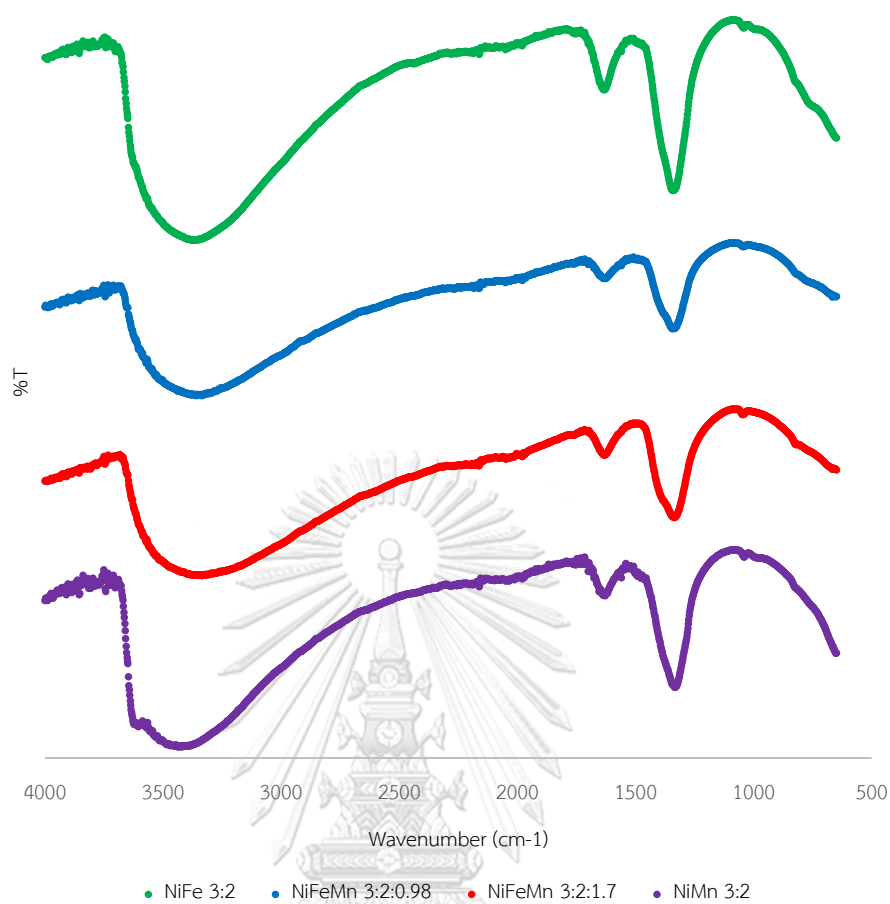
Figure 4.4 The FTIR spectrum of NiFe LDH, NiFeMn LDH 3: 2: 0.98, NiFeMn LDH 3: 2: 1.7, and NiMn LDH

Table 4.2 The FTIR assignment of LDHs

Assignment	Wave number (cm^{-1})				Bond referred
	NiFe LDH 3: 2	NiFeMn LDH 3: 2: 0.98	NiFeMn LDH 3: 2: 1.7	NiMn LDH 3: 2	
OH stretching	3373	3360	3336	3425	M-OH, H_2O
OH bending	1634	1629	1633	1630	M-OH, H_2O
CO_3^{2-} vibrational	1343	1344	1336	1333	CO_3^{2} (interlayer anion)

Electrochemical measurement

Cyclic voltammetry (CV)

According to the literatures [40, 54], LDH gave a pair of redox peaks in cyclic voltammogram which corresponded to the following equation:

$M^{II}(OH)_2 + OH^- \leftrightarrows M^{III}OOH + H_2O + e^-$ [7].

Similarly to the previously reported, results in figure 4.5 showed oxidation peaks of Ni-based LDH around 0.40 V and 0.25 V for reduction, although the oxidation peak
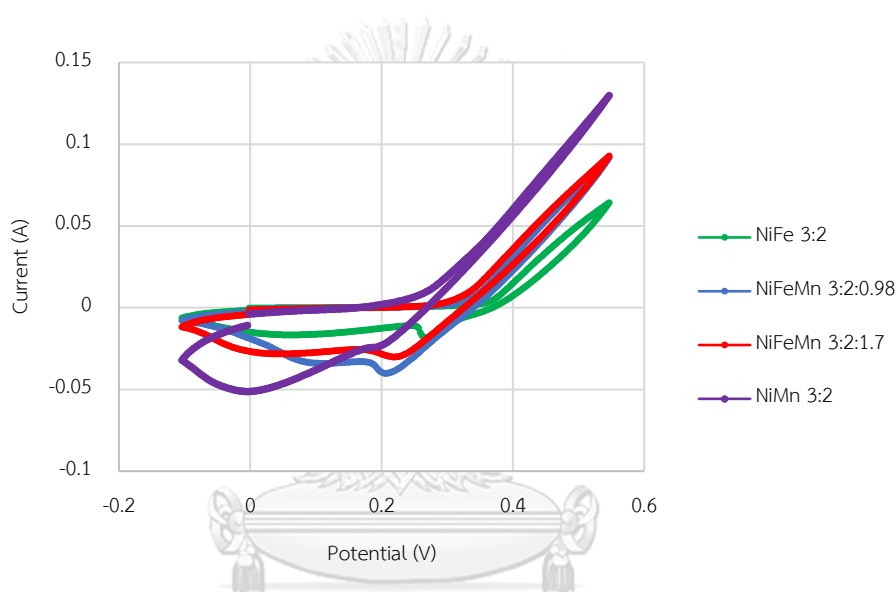

was hindered by background current [59].

Figure 4.5 The 2nd cycle of cyclic voltammetry of NiFe LDH, NiFeMn LDH 3: 2: 0.98, NiFeMn LDH 3: 2: 1.7, and NiMn LDH

To follow the charge of reaction, the overlays of the first, second, and 130th cyclic voltammograms of NiFe LDH 3: 2, NiFeMn LDH 3: 2: 0.98, NiFeMn LDH 3: 2: 1.7, and NiMn LDH 3: 2 were shown in figures 4.6. These cyclic voltammograms revealed peak shifts from cycle to cycle, which indicated a poor contact between LDH and nickel mesh, as LDH eventually peeled off the mesh and redox peak shown was from Ni mesh.

The first cycle was considered as the self-activation process [60-62] while the second cycle showed the highest specific capacity of NiFe-based electrode. Therefore, the second cycle of NiFe LDH, NiFeMn LDH 3: 2: 0.98 and 3: 2: 1.7 (figure 4.7) was chosen for the specific capacity calculation.

The NiFeMn LDH 3: 2: 0.98 and 3: 2: 1.7 gave the specific capacities of 48.58 and 45.86 F/g, respectively. The values were over 2-fold larger than the capacity of pristine NiFe LDH (24.72 F/g). It was noted that, in the first few cycles, NiMn LDH showed higher specific capacity at each cycle and reached the highest capacity of 58.75 F/g at the 14th cycle (figure 4.7). This could be due to the multiple oxidation states of manganese that required longer period of pretreatment.

The specific capacities of the NiFe and Mn-doped NiFe electrode dropped to about 2.5 F/g during the first 10 cycles and stayed at 1 F/g until the 130th cycle. The decrease in capacity as shown in the cyclic voltammograms agreed well with the quasi-reversible property of the redox pair [10]. The structure of LDH might partially transform into metal oxides rather than stay as metal double hydroxides, causing a difficulty in the chemical reversible process. Moreover, the LDH crystal structure swelled and shrank during charge and discharge processes [35], resulting in a peel-off of LDH from Ni mesh.
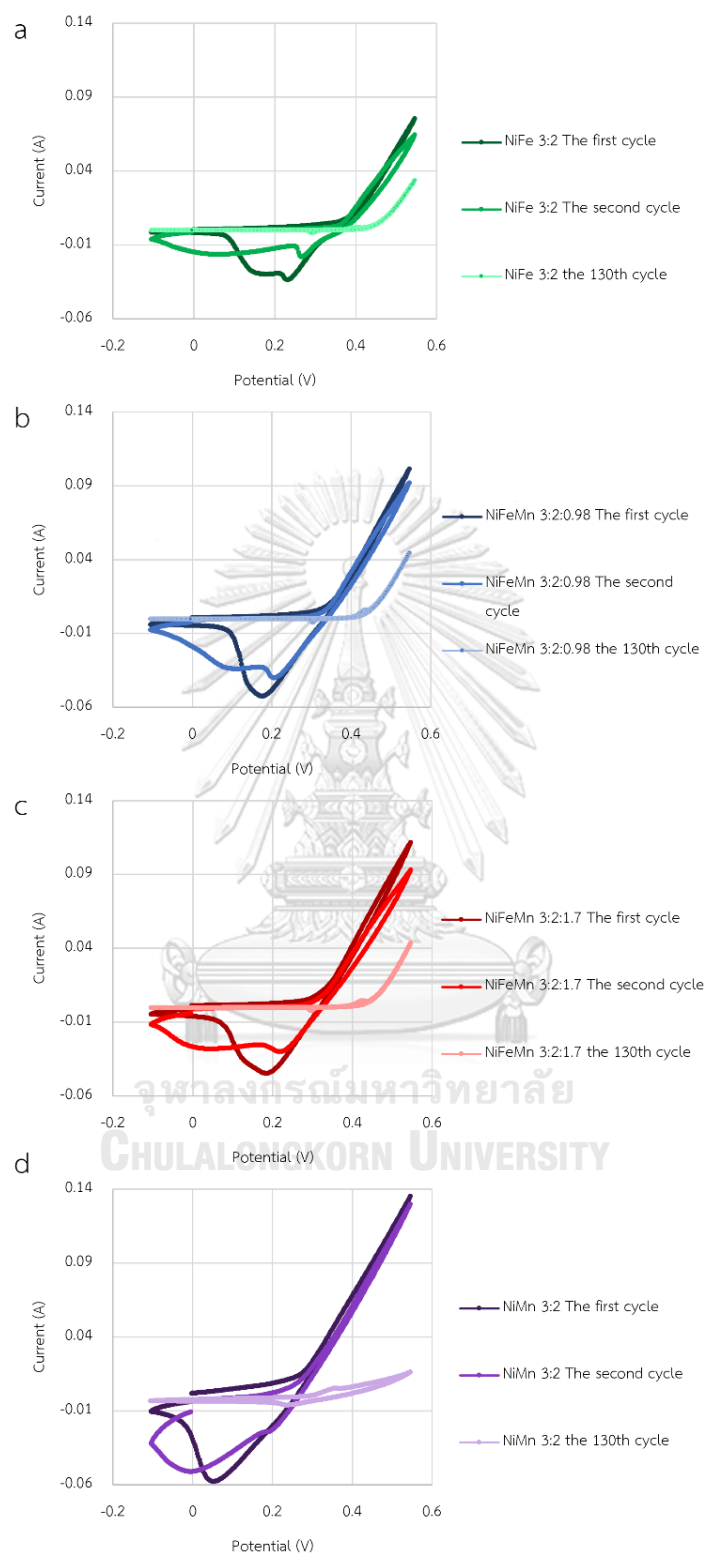
Figure 4.6 The cyclic voltammograms of the first, second, and 130th cycles of
a) NiFe LDH, b) NiFeMn LDH 3: 2: 0.98, c) NiFeMn LDH 3: 2: 1.7, and d) NiMn LDH
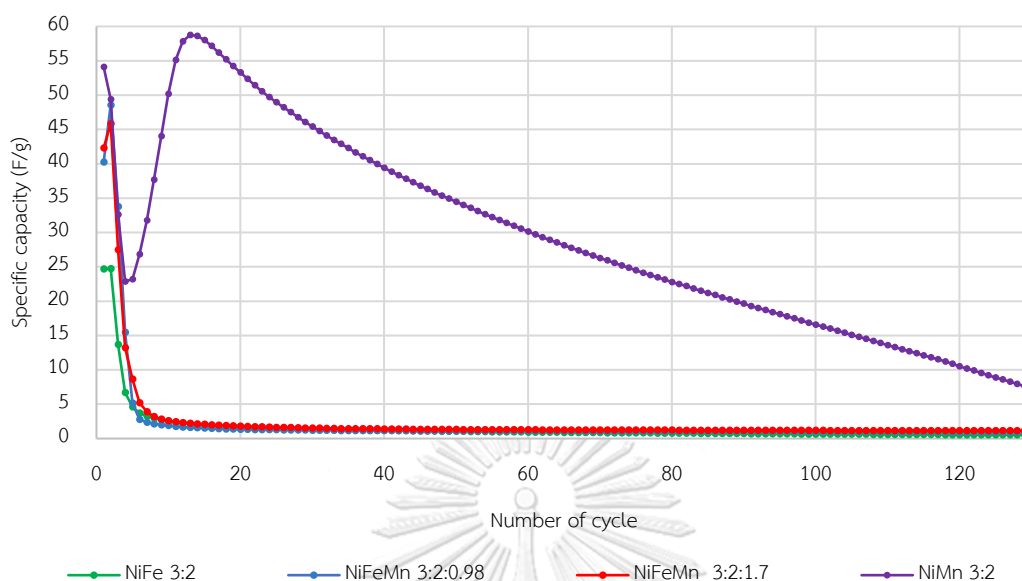
Figure 4.7 The cycling performance of the electrodes: NiFe LDH,
NiFeMn LDH 3: 2: 0.98, NiFeMn LDH 3: 2: 1.7, and NiMn LDH, by cyclic voltammetry

Galvanostatic charge discharge (GCD)

The galvanostatic charge-discharge was performed at 0.1 A/g, and the charging time was fixed at 1000 seconds. The first cycle of NiFe LDH, NiFeMn LDH 3: 2: 0.98 and NiFeMn LDH 3: 2: 1.7 delivered resemblant capacities of 65.84, 57.73 and 57.79 F/g, respectively (figure 4.8).

Plateaus in figure 4.8 suggested complete separation of redox peaks [51, 63], which was a characteristic of faradaic behavior [51, 64] due to the quasi reversible of LDH [65]. This voltage was related to reduction potential, as shown in CV. NiMn LDH had much lower reduction potential compared to NiFe LDH. This was related to experimental plateau of voltage that appeared around 0.2-0.3 V. As the amount of Mn in LDH structure increased, the recorded potential decreased.

Figure 4.8 The first curves of galvanostatic charge discharge of NiFe LDH,
NiFeMn LDH 3: 2: 0.98, NiFeMn LDH 3: 2: 1.7, and NiMn LDH

NiFe LDH was not completely reversible due to its high resistivity, resulting in a reduced number of active sites. As shown in the fifth cycle (figure 4.9), Mn-doped NiFe LDH showed higher specific capacity compared to pristine NiFe LDH.
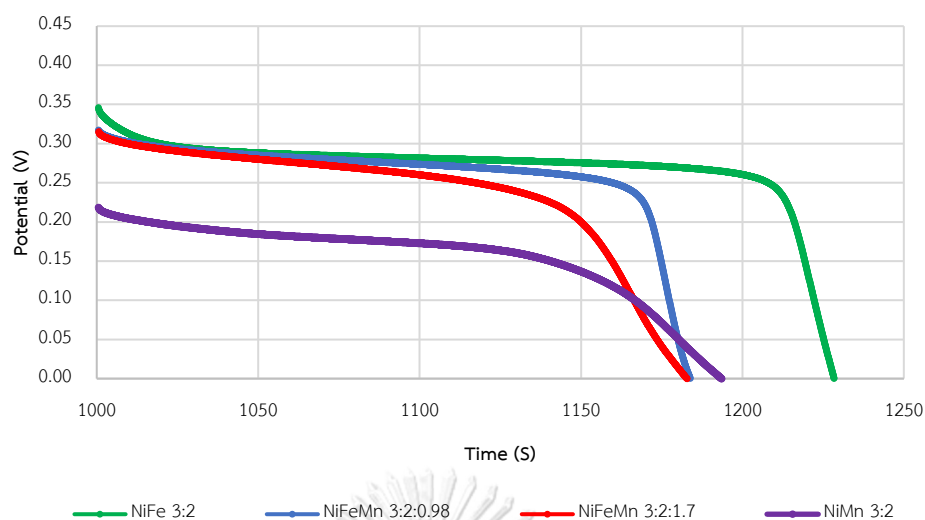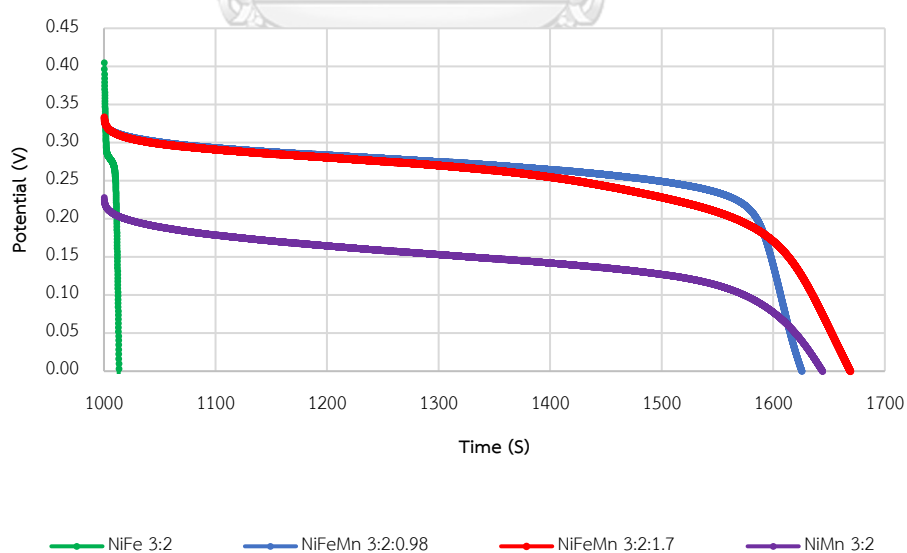

Figure 4.9 The fifth curve of galvanostatic charge discharge of NiFe LDH,
NiFeMn LDH 3: 2: 0.98, NiFeMn LDH 3: 2: 1.7, and NiMn LDH

The electrode was charged and discharged for 40 cycles during the cycling test. The highest specific capacities from galvanostatic charge discharge were 207.6 F/g at the 6th cycle of NiFeMn LDH 3: 2: 1.7 and 203.6 F/g at the 7th cycle of NiFeMn LDH 3: 2: 0.98. The values were about 2.3 times greater than those of NiFe LDH (89.32 F/g). Due to a peeling off of the active materials during the charge discharge experiments, a decrease in a specific capacity was observed. Therefore, the cycling performance was reported up to the 10th cycle (figure 4.10).
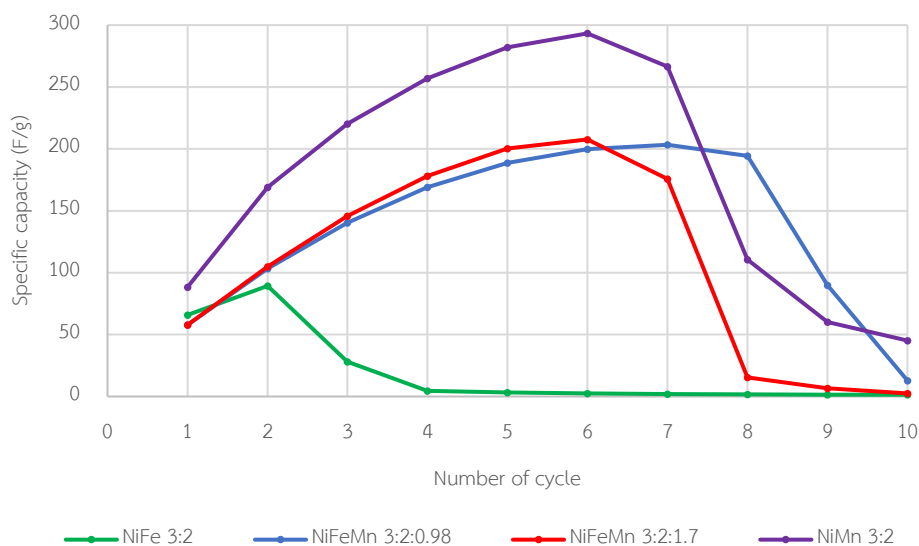
Figure 4.10 The cycling performance of the electrode: NiFe LDH, NiFeMn LDH 3: 2: 0.98, NiFeMn LDH 3: 2: 1.7, and NiMn LDH by galvanostatic charge discharge

Both CV and GCD results showed an increasing in specific capacities. This could be due to the presence of manganese. Previous report revealed the co-existing oxidation states of Mn^{2+}, Mn^{3+}, and Mn^{4+} in NiFeMn LDH with the most existing ratio of Mn^{3+} [66]. Mn^{3+} played an important role because it was an intermediate state between Mn^{2+} and Mn^{4+} as the followings:

$$Mn^{2+} + OH^- \rightleftharpoons Mn^{3+} + e^- + H_2O \text{ and}$$

$$Mn^{3+} + OH^- \rightleftharpoons Mn^{4+} + e^- + H_2O$$
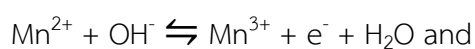
,which could increase the transformation rate of Mn^{2+}/Mn^{4+} couples [15].

Electrical measurements

Current-voltage relationship analysis

As shown in figure 4.11, the current voltage relationship revealed a resistance (R) value through the slope (slope=1/R). At initial state (1-5 V), the resistivity ($\boldsymbol{\rho}$) of NiFeMn LDH and NiFe LDH were 2.76×10^5 Ωm and 2.23×10^6 Ωm, respectively. As previously reported, high conductivity significantly boosted a specific capacity of cathode via electron transfer [54]. The decrease in resistance due to Mn doping agreed well with the increase in specific capacity. However, after a period of time, the relationship between current and voltage did not follow a linear trend. Thus, the EIS was more appropriate for the resistance determination.
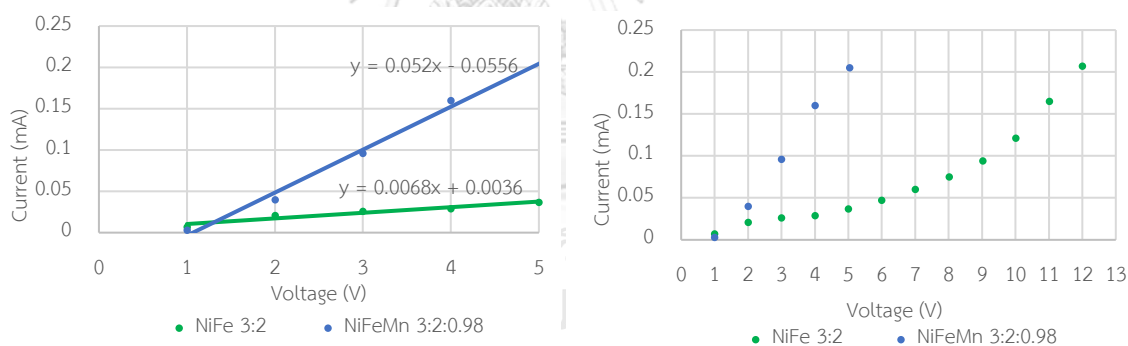
Figure 4.11 The current voltage relationship of NiFe LDH 3: 2 and
NiFeMn LDH 3: 2: 0.98

Electrochemical impedance spectroscopy (EIS)

As indicated in the Nyquist plot, all resistances were reduced after Mn doping (figure 4.12). Doped LDHs had ohmic resistances (R_s) of 197.3 Ω and 169.2 Ω, which were 5 times lower than NiFe LDH. The NiFeMn LDH 3: 2: 0.98 revealed a charge transfer resistance (R_{ct}) of 2661 Ω, which was about half of the undoped LDH

(4102 Ω) (as summarized in table 4.3). Furthermore, charge transfer resistance was undetectable in NiFeMn LDH 3: 2: 1.7. This agreed well with the high rate of reaction due to the enhancement of electron transfer. As previously discussed, Mn^{3+}, which served as an intermediate in NiFeMn LDH, could increase the rate of redox reaction. Similarly, in both current-voltage relationship analysis and electrochemical impedance spectroscopy (EIS), doping manganese in NiFe LDH resulted in a resistance diminution. As seen in table 4.3, increasing in conductivity could relate to the enhancement of a specific capacity [67].
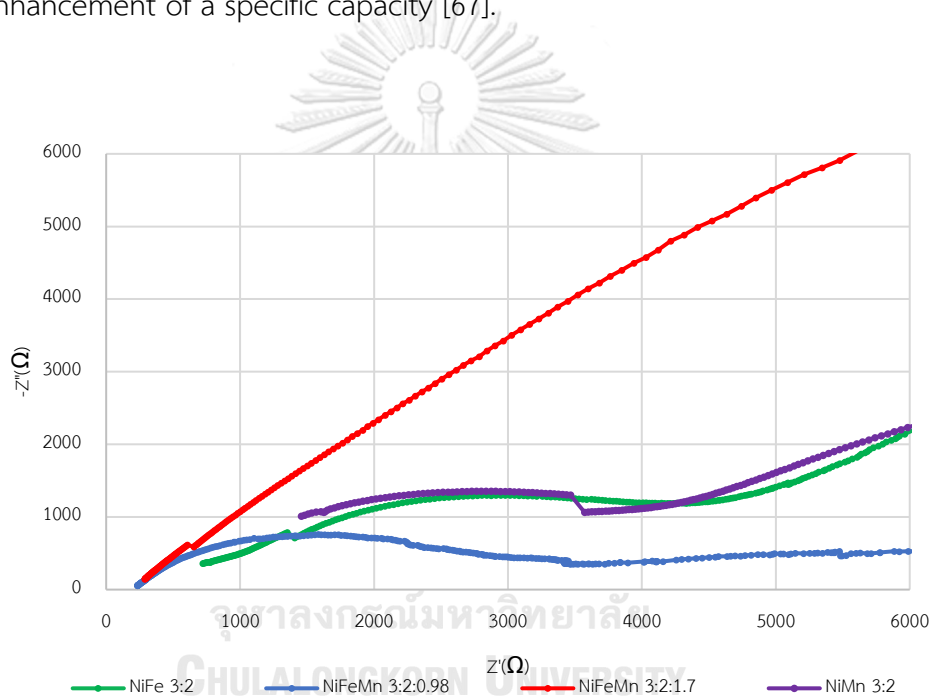
Figure 4.12 The Nyquist plot of NiFe LDH, NiFeMn LDH 3: 2: 0.98, NiFeMn LDH 3: 2: 1.7, and NiMn LDH

Table 4.3 The summary of LDH performance and resistances

	The highest specific capacity from each method		Electrochemical impedance spectroscopy (EIS)	
	CV (F/g)	GCD (F/g)	R_s (Ω)	R_{ct} (Ω)
NiFe LDH	24.72	89.32	889.9	4102
NiFeMn LDH 3: 2: 0.98	48.58	203.3	197.3	2661
NiFeMn LDH 3: 2: 1.7	45.86	207.6	169.2	ND
NiMn LDH	58.75	293.3	375.0	4903

The key mechanism of charging LDH was a change in oxidation states, from Ni^{2+} to Ni^{3+}. Metal doping could lower energy gap of pristine compounds because the additional orbitals created intermediate levels for electron transfer. The energy levels of oxygen p-orbitals and metal d-orbitals of several metal oxides were shown in figure 4.13 [33, 68]. These energy levels of metal oxides could be used as a guidance to the conduction bands and valence bands of LDH. Because of Mn doping, orbitals of these valence bands and conduction bands overlapped, and the energy barrier between the highest occupied band and the lowest unoccupied band was reduced, resulting in lower Gibbs free energy needed for the electron transfer in NiFeMn LDH compared to $Ni(OH)_2$ and $NiFe(OH)_2$ [33].
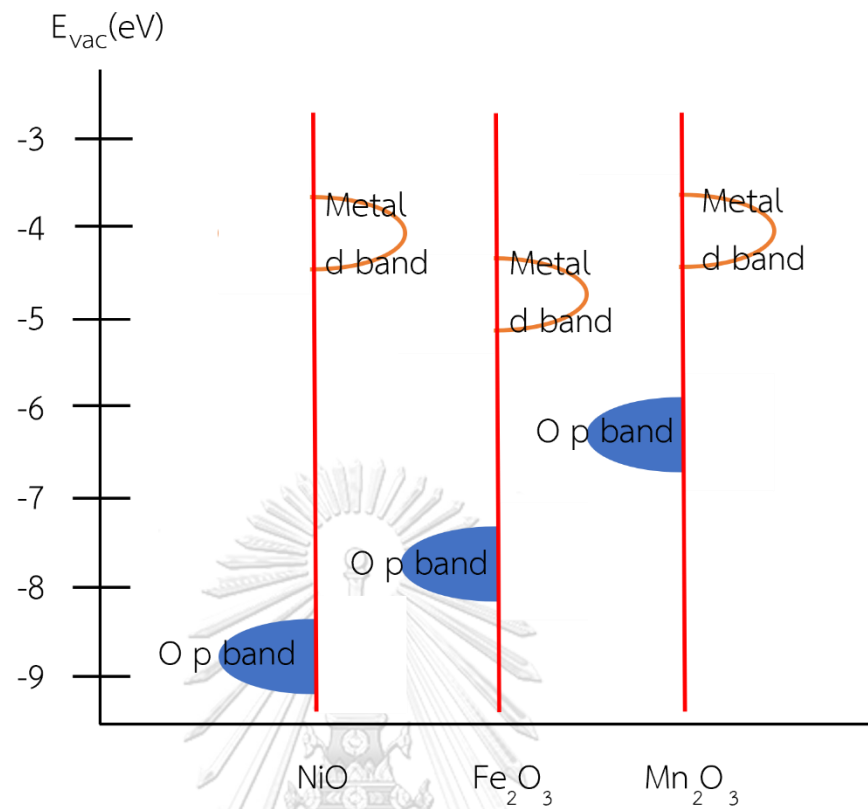
Figure 4.13 The energy level of metal oxide

CHAPTER 5 CONCLUSION

Mn-doped NiFe LDHs with different Mn: Fe ratios were successfully synthesized using coprecipitation method in mild conditions. The experimental ratios of NiFe LDH 3: 1, NiFeMn LDH 3: 1: 0.5, NiFeMn LDH 3: 1: 1, and NiMn LDH 3: 1 were found to be 3: 2, 3: 2: 1.70, 3: 2: 0.98, and 3: 2, respectively. Despite that the exact ratio of LDH from ICP was not equal to the calculated ratio, XRD confirmed the single phase of LDH structure. Although, doping manganese did not affect the crystal structure of LDH, it lowered the crystallinity. Moreover, SEM-EDX showed homogenous distribution of all metals in the LDH structures. FTIR showed LDH functional group in all synthesized LDHs.

The electrode was prepared by casting LDH: carbon black: PVdF 8: 1: 1 on Ni-mesh. After Mn doping, the CV exhibited an increase in specific capacity. According to the GCD technique, the highest specific capacity of Mn-doped NiFe LDH 3: 2: 1.7 was 207.6 F/g, whereas the 3: 2: 0.98 exhibited 203.3 F/g. Both of the Mn-doped LDH did not show a difference in capacity. The specific capacity was related to the decrease in resistance due to the Mn doping. In Mn-doped NiFe LDH, the specific capacity increased while the ohmic resistance and charge transfer resistance decreased. Ohmic resistance was decreased over 4.5 times, and charge transfer resistance was not detected in NiFeMn 3: 2: 1.7.

These results confirm the role of intermediate oxidation state species that could lower the resistivity by increasing the electron transfer rate. The scope of research can be explored using a variety of ratios of Ni: Fe: Mn or using other conductive elements. In addition, non-reusable current collector such as Ni foam can be used to decrease diffusion path, otherwise ohmic resistance (R_s) has to be considered [69].

There are two suggested characterization methods. First, the oxidation state of all metals can be evaluated by X-ray photoelectron spectroscopy (XPS). This can show the role of each metal in the charging mechanism. Second, the band overlap can be calculated from a density of state graph obtained from the density functional theory (DFT).

This work contributes as a guidance for the development of energy storage materials because manganese can increase specific capacitor while its voltage remains as same as NiFe LDH. This is a benefit for wide voltage windows with high specific capacity energy storage. Mixed metals, which include low-cost and environmental friendly metals, will be a desirable fundamental in the development of energy storage.

REFERENCES

[1] Han, B., Cheng, G., Zhang, E.Y.Y., Zhang, L.J., and Wang, X.K. Three dimensional hierarchically porous ZIF-8 derived carbon/LDH core-shell composite for high performance supercapacitors. Electrochimica Acta 263 (2018): 391-399.

[2] Wang, B., et al. Hierarchical NiAl layered double hydroxide/multiwalled carbon nanotube/nickel foam electrodes with excellent pseudocapacitive properties. Acs Applied Materials & Interfaces 6(18) (2014): 16304-16311.

[3] Wang, W.C., et al. Preparation of Ni-Al layered double hydroxide hollow microspheres for supercapacitor electrode. Chemical Engineering Journal 338 (2018): 55-61.

[4] Long, D.F., Liu, H.J., Yuan, Y., Li, J.P., Li, Z., and Zhu, J.L. A facile and large-scale synthesis of NiCo-LDHs@rGO composite for high performance asymmetric supercapacitors. Journal of Alloys and Compounds 805 (2019): 1096-1105.

[5] Sanati, S. and Rezvani, Z. Ultrasound-assisted synthesis of NiFe- layered double hydroxides as efficient electrode materials in supercapacitors. Ultrasonics Sonochemistry 48 (2018): 199-206.

[6] Sim, H., et al. Reverse micelle synthesis of colloidal nickel–manganese layered double hydroxide nanosheets and their pseudocapacitive properties. Chemistry – A European Journal 20(45) (2014): 14880-14884.

[7] Li, X., Du, D., Zhang, Y., Xing, W., Xue, Q., and Yan, Z. Layered double hydroxides toward high-performance supercapacitors. Journal of Materials Chemistry A 5(30) (2017): 15460-15485.

[8] Fang, X., Han, S., Liu, D., and Zhu, Y. Two-dimensional CoFe hydroxides nanostructure as positive material for asymmetric supercapacitor. Chemical Physics Letters 746 (2020): 137282.

[9] Guo, X.L., et al. Nickel-Manganese layered double hydroxide nanosheets supported on nickel foam for high-performance supercapacitor electrode materials. Electrochimica Acta 194 (2016): 179-186.

[10]   Lu, Y., et al. An investigation of ultrathin nickel-iron layered double hydroxide nanosheets grown on nickel foam for high-performance supercapacitor electrodes. Journal of Alloys and Compounds 714 (2017): 63-70.

[11]   Zhao, J., et al. CoMn-layered double hydroxide nanowalls supported on carbon fibers for high-performance flexible energy storage devices. Journal of Materials Chemistry A 1(31) (2013): 8836-8843.

[12]   Ma, K., Cheng, J.P., Liu, F., and Zhang, X. Co-Fe layered double hydroxides nanosheets vertically grown on carbon fiber cloth for electrochemical capacitors. Journal of Alloys and Compounds 679 (2016): 277-284.

[13]   Singh, S., et al. Tailoring the morphology followed by the electrochemical performance of NiMn-LDH nanosheet arrays through controlled Co-doping for high-energy and power asymmetric supercapacitors. Dalton Transactions 46(38) (2017): 12876-12883.

[14]   Shang, Y.Z., Ma, S., Wei, Y.M., Yang, H., and Xu, Z.L. Flower-like ternary metal of Ni-Co-Mn hydroxide combined with carbon nanotube for supercapacitor. Ionics 26(7) (2020): 3609-3619.

[15]   Cao, J.M., et al. Mn-doped Ni/Co LDH nanosheets grown on the natural N-dispersed PANI-derived porous carbon template for a flexible asymmetric supercapacitor. Acs Sustainable Chemistry & Engineering 7(12) (2019): 10699-10707.

[16]   https://www.clarke-energy.com/energy-storage/.

[17]   Bailera, M., Lisbona, P., Romeo, L.M., and Espatolero, S. Power to Gas projects review: Lab, pilot and demo plants for storing renewable energy and CO2. Renewable and Sustainable Energy Reviews 69 (2017): 292-312.

[18]   Conway, B.E. Electrochemical supercapacitors : scientific fundamentals and technological applications. New York: Plenum Press, 1999.

[19]   Huggins, R.A. Energy storage. New York: Springer, 2010.

[20]   https://mechatrofice.com/electrical/capacitor-function-induction-motor.

[21]   https://www.arrow.com/en/research-and-events/articles/capacitor-banks-benefit-an-energy-focused-world.

[22]   Vangari, M., Pryor, T., and Jiang, L. Supercapacitors: Review of Materials and Fabrication Methods. Journal of Energy Engineering 139(2) (2013): 72-79.

[23]   Brousse, T., Bélanger, D., and Long, J.W. To Be or Not To Be Pseudocapacitive? Journal of The Electrochemical Society 162(5) (2015): A5185-A5189.

[24]   Choudhary, N., et al. Asymmetric Supercapacitor Electrodes and Devices. Advanced Materials 29(21) (2017): 1605336.

[25]   Shao, Y., et al. Design and Mechanisms of Asymmetric Supercapacitors. Chemical Reviews 118(18) (2018): 9233-9280.

[26]   Afif, A., Rahman, S.M.H., Tasfiah Azad, A., Zaini, J., Islan, M.A., and Azad, A.K. Advanced materials and technologies for hybrid supercapacitors for energy storage – A review. Journal of Energy Storage 25 (2019): 100852.

[27]   Zhong, C., Deng, Y., Hu, W., Qiao, J., Zhang, L., and Zhang, J. A review of electrolyte materials and compositions for electrochemical supercapacitors. Chemical Society Reviews 44(21) (2015): 7484-7539.

[28]   Liu, X., et al. Ultrahigh-rate-capability of a layered double hydroxide supercapacitor based on a self-generated electrolyte reservoir. Journal of Materials Chemistry A 4(21) (2016): 8421-8427.

[29]   Fan, G., Li, F., Evans, D.G., and Duan, X. Catalytic applications of layered double hydroxides: recent advances and perspectives. Chemical Society Reviews 43(20) (2014): 7040-7066.

[30]   Sun, X., Wang, G.K., Sun, H.T., Lu, F.Y., Yu, M.P., and Lian, J. Morphology controlled high performance supercapacitor behaviour of the Ni-Co binary hydroxide system. Journal of Power Sources 238 (2013): 150-156.

[31]   Chen, G., et al. Microwave-assisted synthesis of hybrid CoxNi1−x(OH)2 nanosheets: Tuning the composition for high performance supercapacitor. Journal of Power Sources 251 (2014): 338-343.

[32]   Xue, X., et al. One-step synthesis of nickel–iron layered double hydroxides with tungstate acid anions via flash nano-precipitation for the oxygen evolution reaction. Sustainable Energy & Fuels 3(1) (2019): 237-244.

[33]   Zhang, Y., et al. Unveiling the critical role of the Mn dopant in a NiFe(OH)2 catalyst for water oxidation. Journal of Materials Chemistry A 8(34) (2020): 17471-17476.

[34]   Mishra, G., Dash, B., and Pandey, S. Layered double hydroxides: A brief review from fundamentals to application as evolving biomaterials. Applied Clay Science 153 (2018): 172-186.

[35]   Zhang, Y.Q. and Wei, S. Mg-Co-Al-LDH nanoparticles with attractive electrochemical performance for supercapacitor. Journal of Nanoparticle Research 21(1) (2019): 14.

[36]   Sarfraz, M. and Shakir, I. Recent advances in layered double hydroxides as electrode materials for high-performance electrochemical energy storage devices. Journal of Energy Storage 13 (2017): 103-122.

[37]   Zou, W.R., et al. Anion exchange of Ni-Co layered double hydroxide (LDH) nanoarrays for a high-capacitance supercapacitor electrode: A comparison of alkali anion exchange and sulfuration. Chemistry-a European Journal 24(72) (2018): 19309-19316.

[38]   Zhu, F.F., Liu, W.J., Liu, Y., and Shi, W.D. Construction of porous interface on CNTs@NiCo-LDH core-shell nanotube arrays for supercapacitor applications. Chemical Engineering Journal 383 (2020).

[39]   Hua, X., Mao, C.J., Chen, J.S., Chen, P.P., and Zhang, C.F. Facile synthesis of new-type MnOOH/NiAl-layered double hydroxide nanocomposite for high-performance supercapacitor. Journal of Alloys and Compounds 777 (2019): 749-758.

[40]   Xu, X.W., et al. Integrated energy aerogel of N,S-rGO/WSe2/NiFe-LDH for both energy conversion and storage. Acs Applied Materials & Interfaces 9(38) (2017): 32756-32766.

[41]   Liu, H.B., Xiang, L., and Jin, Y. Hydrothermal modification and characterization of Ni(OH)2 with high discharge capability. Crystal Growth & Design 6(1) (2006): 283-286.

[42]   Warsi, M.F., Shakir, I., Shahid, M., Sarfraz, M., Nadeem, M., and Gilani, Z.A. Conformal coating of cobalt-nickel layered double hydroxides nanoflakes on carbon fibers for high-performance electrochemical energy storage supercapacitor devices. Electrochimica Acta 135 (2014): 513-518.

[43]   Liu, X.-M., Zhang, Y.-H., Zhang, X.-G., and Fu, S.-Y. Studies on Me/Al-layered double hydroxides (Me = Ni and Co) as electrode materials for electrochemical capacitors. Electrochimica Acta 49(19) (2004): 3137-3141.

[44]   Lamdab, U., Wetchakun, K., Kangwansupamonkon, W., and Wetchakun, N. Effect of a pH-controlled co-precipitation process on rhodamine B adsorption of MnFe2O4 nanoparticles. RSC Advances 8(12) (2018): 6709-6718.

[45]   Yan, A.-L., Wang, X.-C., and Cheng, J.-P. Research Progress of NiMn Layered Double Hydroxides for Supercapacitors: A Review. Nanomaterials 8(10) (2018).

[46]   Cherevko, S. and Mayrhofer, K.J.J. On-Line Inductively Coupled Plasma Spectrometry in Electrochemistry: Basic Principles and Applications. in, 2018.

[47]   Pecharsky, V.K. Fundamentals of powder diffraction and structural characterization of materials, ed. Zavalij, P.Y. Boston [Mass.]

London: Kluwer Academic Publishers, 2003.

[48]   Sutton, M.A., Li, N., Joy, D.C., Reynolds, A.P., and Li, X. Scanning Electron Microscopy for Quantitative Small and Large Deformation Measurements Part I: SEM Imaging at Magnifications from 200 to 10,000. Experimental Mechanics 47(6) (2007): 775-787.

[49]   Jafari, M.A. Application of Vibrational Spectroscopy in Organic Electronics. in, 2017.

[50]

chem.libretexts.org/Bookshelves/Organic_Chemistry/Book%3A_Organic_Chemi stry_with_a_Biological_Emphasis_v2.0_(Soderberg)/04%3A_Structure_Determin ation_I-_UV-
Vis_and_Infrared_Spectroscopy_Mass_Spectrometry/4.04%3A__Infrared_spectr oscopy.

[51] Mathis, T.S., Kurra, N., Wang, X., Pinto, D., Simon, P., and Gogotsi, Y. Energy Storage Data Reporting in Perspective—Guidelines for Interpreting the Performance of Electrochemical Energy Storage Systems. Advanced Energy Materials 9(39) (2019): 1902007.

[52] Kim, T., et al. Applications of Voltammetry in Lithium Ion Battery Research. J. Electrochem. Sci. Technol 11(1) (2020): 14-25.

[53] https://www.gamry.com/application-notes/battery-research/testing-electrochemical-capacitors-cyclic-voltammetry-leakage-current/.

[54] Wang, F., Wang, T., Sun, S., Xu, Y., Yu, R., and Li, H. One-step synthesis of Nickle Iron-layered double hydroxide/reduced graphene oxide/carbon nanofibres composite as electrode materials for asymmetric supercapacitor. Scientific Reports 8(1) (2018): 8908.

[55] Grossi, M. and Riccò, B. Electrical impedance spectroscopy (EIS) for biological analysis and food characterization: a review. Journal of Sensors and Sensor Systems 6 (2017): 303-325.

[56] Jossen, A. BATTERIES | Dynamics. in Garche, J. (ed.)Encyclopedia of Electrochemical Power Sources, pp. 478-488. Amsterdam: Elsevier, 2009.

[57] Li, H., Musharavati, F., Zalenezhad, E., Chen, X., Hui, K.N., and Hui, K.S. Electrodeposited NiCo layered double hydroxides on titanium carbide as a binder-free electrode for supercapacitors. Electrochimica Acta 261 (2018): 178-187.

[58] Iqbal, M.A., Asghar, H., and Fedel, M. Ce-Doped-MgAl Superhydrophobic Layered Double Hydroxide for Enhanced Corrosion Resistance Properties. Solids 2(1) (2021): 76-86.

[59] Jensen, J.R. Transition metal layered double hydroxides for energy storage. Queensland University of Technology, 2015.

[60] Lu, X., et al. Facile synthesis of large-area manganese oxide nanorod arrays as a high-performance electrochemical supercapacitor. Energy & Environmental Science 4(8) (2011): 2915-2921.

[61]   Yuan, L., Yao, B., Hu, B., Huo, K., Chen, W., and Zhou, J. Polypyrrole-coated paper for flexible solid-state energy storage. Energy & Environmental Science 6(2) (2013): 470-476.

[62]   Yang, G., Takei, T., Yanagida, S., and Kumada, N. Enhanced Supercapacitor Performance Based on CoAl Layered Double Hydroxide-Polyaniline Hybrid Electrodes Manufactured Using Hydrothermal-Electrodeposition Technology. Molecules 24(5) (2019).

[63]   Jiang, Y. and Liu, J. Definitions of Pseudocapacitive Materials: A Brief Review. ENERGY & ENVIRONMENTAL MATERIALS 2(1) (2019): 30-37.

[64]   Lan, Y., et al. Phosphorization boosts the capacitance of mixed metal nanosheet arrays for high performance supercapacitor electrodes. Nanoscale 10(25) (2018): 11775-11781.

[65]   Zhang, L., Hui, K.N., Hui, K.S., Chen, X., Chen, R., and Lee, H. Role of graphene on hierarchical flower-like NiAl layered double hydroxide-nickel foam-graphene as binder-free electrode for high-rate hybrid supercapacitor. International Journal of Hydrogen Energy 41(22) (2016): 9443-9453.

[66]   Wang, G., Li, D., Wang, S., Zhao, Z., Lv, S., and Qiu, J. Ternary NiFeMn layered metal oxide (LDO) compounds for capacitive deionization defluoridation: The unique role of Mn. Separation and Purification Technology 254 (2021): 117667.

[67]   Kumar, K.S., Choudhary, N., Jung, Y., and Thomas, J. Recent Advances in Two-Dimensional Nanomaterials for Supercapacitor Electrode Applications. ACS Energy Letters 3(2) (2018): 482-495.

[68]   Liao, C., Li, Y., and Tjong, S.C. Visible-Light Active Titanium Dioxide Nanomaterials with Bactericidal Properties. Nanomaterials 10(1) (2020).

[69]   Salleh, N.A., Kheawhom, S., and Mohamad, A.A. Characterizations of nickel mesh and nickel foam current collectors for supercapacitor application. Arabian Journal of Chemistry 13(8) (2020): 6838-6846.

CHAPTER 6 APPENDIX

Calculated weights used for the synthesis of LDHs in this work were shown in table 6.1.

Table 6.1 Theoretical weights of metal nitrate

LDH ratio	theoretical weight (g)		
	$Ni(NO_3)_2 \cdot 6H_2O$	$Fe(NO_3)_3 \cdot 9H_2O$	$Mn(NO_3)_2 \cdot 4H_2O$
NiFe 3: 1 LDH	2.7405	2.0200	-
NiFeMn 3: 1: 0.5 LDH	2.7405	2.0200	0.6274
NiFeMn 3: 1: 1 LDH	2.7405	2.0200	1.2548
NiMn 3: 1 LDH	2.7405	-	1.2548

ICP calibration curves between intensity and concentration (mM) were shown in figure 6.1.
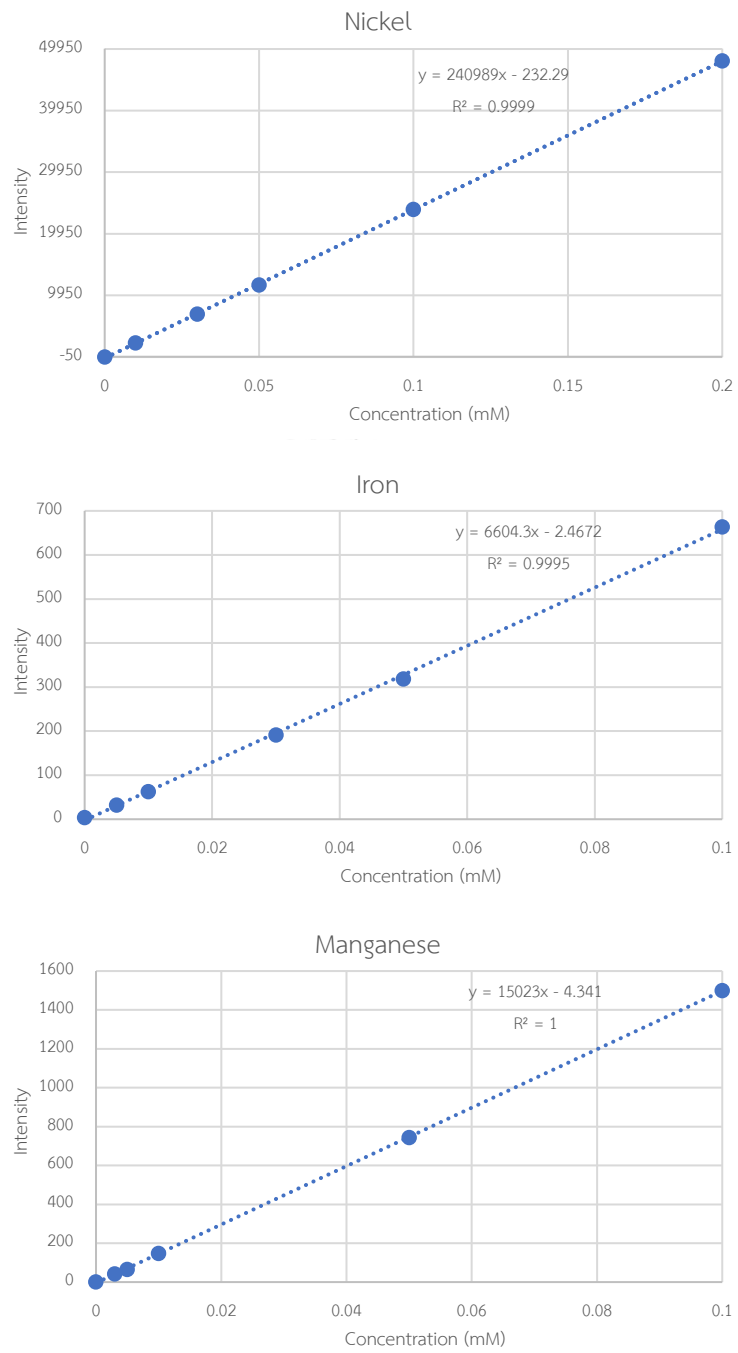
Figure 6.1 The calibration curves of nickel, iron and manganese

Specific capacity from cyclic voltammetry was calculated as shown below.
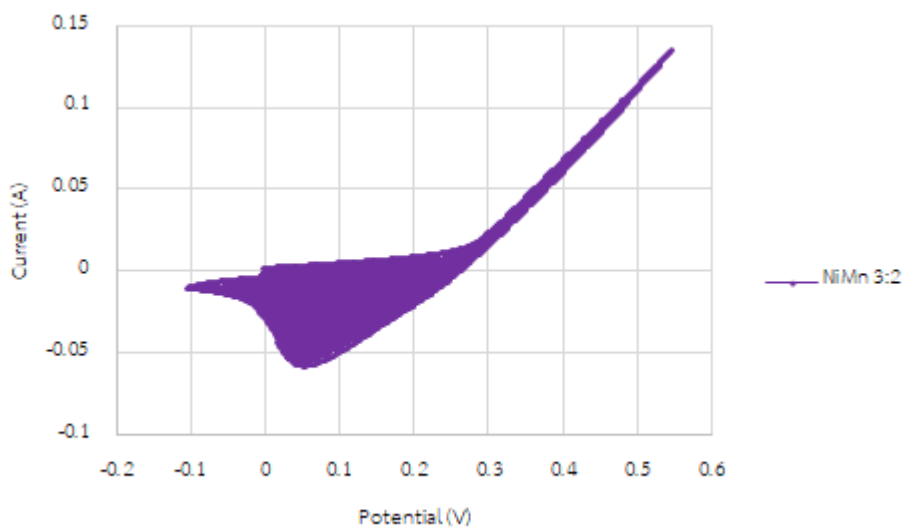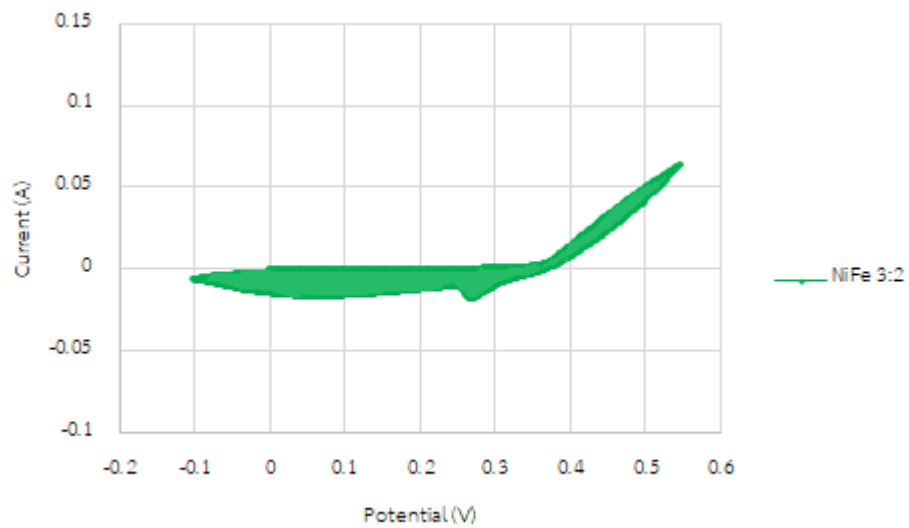
1st cycle (pre-treat)
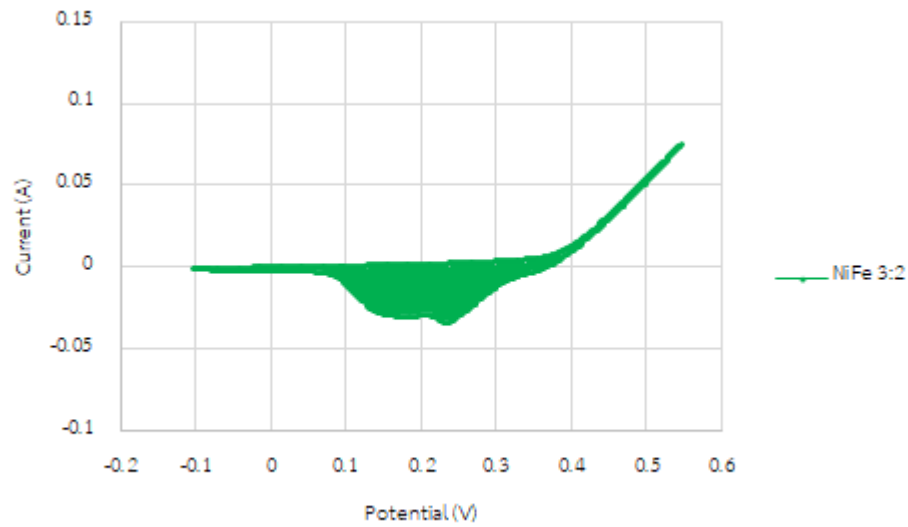
Figure 6.2 The 1st cyclic voltammogram of NiFe LDH

Area = 0.007140 AV

LDH mass (active mass) = 0.0223 g

Scan rate = 0.01 V/s

$$C_p = \frac{A}{2(V_2-V_1)mk}$$

$$C_p = \frac{0.007140}{2*(0.55-(-0.1))*0.0223*0.01}$$

$$C_p = 24.68 \text{ F/g}$$
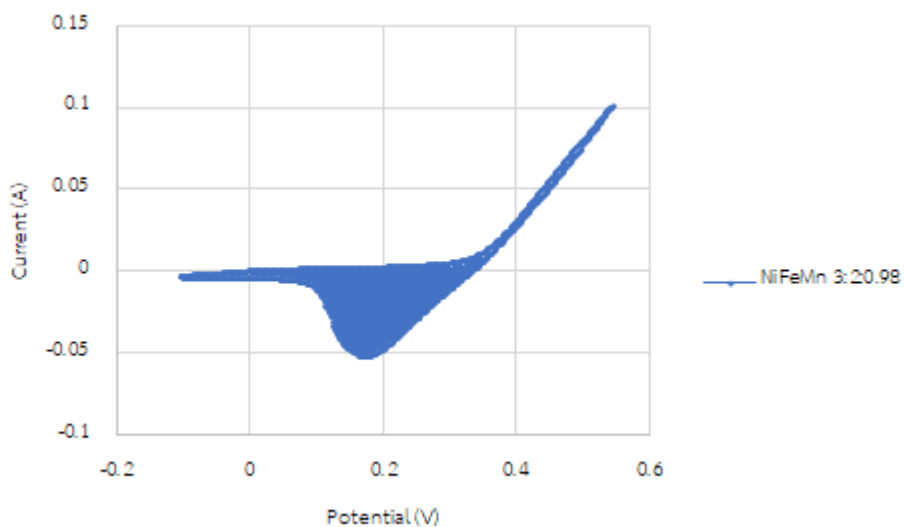
Figure 6.3 The 1st cyclic voltammogram of NiFeMn LDH 3: 2: 0.98

Area = 0.009713 AV

LDH mass (active mass) = 0.0186 g

Scan rate = 0.01 V/s

$$C_p = \frac{A}{2(V_2-V_1)mk}$$

$$C_p = \frac{0.009713}{2*(0.55-(-0.1))*0.0186*0.01}$$
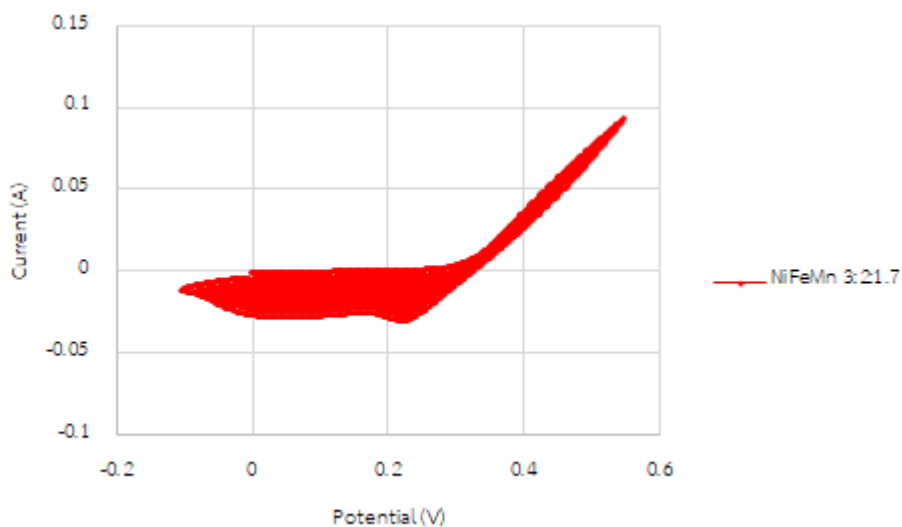
$$C_p = 40.24 \text{ F/g}$$
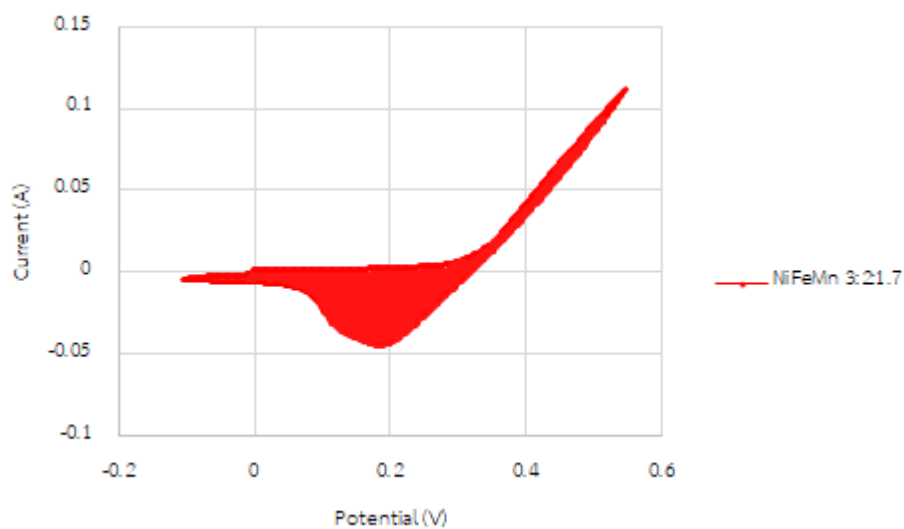
Figure 6.4 The 1st cyclic voltammogram of NiFeMn LDH 3: 2: 1.7

Area = 0.01018 AV

LDH mass (active mass) = 0.0185 g

Scan rate = 0.01 V/s

$$C_p = \frac{A}{2(V_2 - V_1)mk}$$

$$C_p = \frac{0.01018}{2*(0.55-(-0.1))*0.0185*0.01}$$
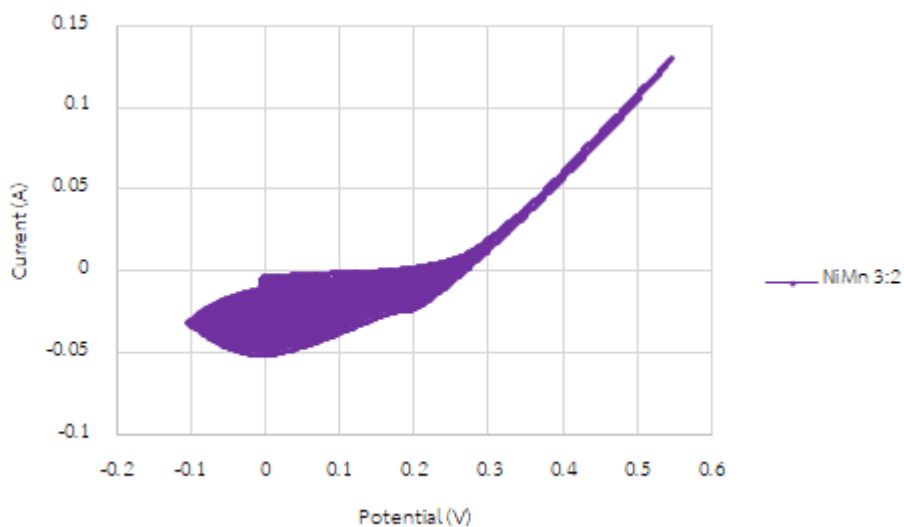
$$C_p = 42.32 \ F/g$$

Figure 6.5 The 1st cyclic voltammogram of NiMn LDH

Area = 0.01356 AV
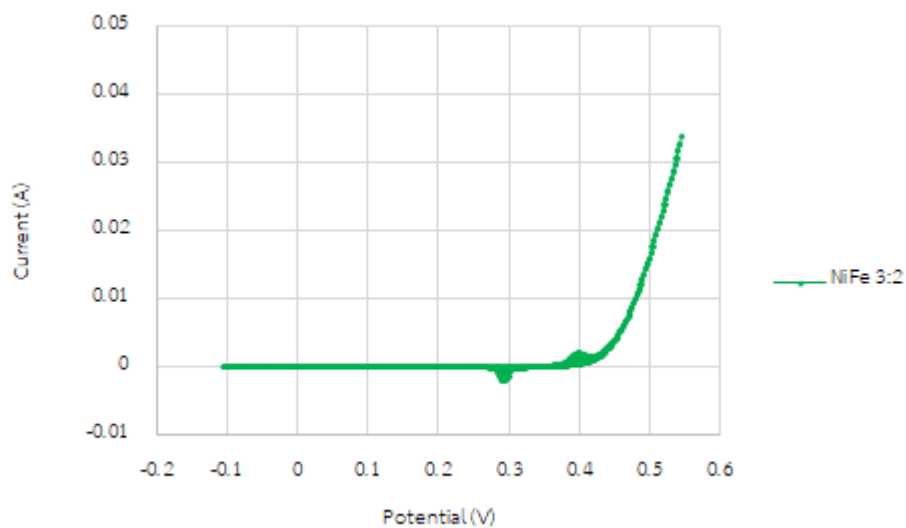
LDH mass (active mass) = 0.0193 g

Scan rate = 0.01 V/s

$$C_p = \frac{A}{2(V_2-V_1)mk}$$

$$C_p = \frac{0.01356}{2*(0.55-(-0.1))*0.0193*0.01}$$

$$C_p = 54.12 \text{ F/g}$$

2nd cycle

Figure 6.6 The 2nd cyclic voltammogram of NiFe LDH

Area = 0.007154 AV

LDH mass (active mass) = 0.0223 g

Scan rate = 0.01 V/s

$$C_p = \frac{A}{2(V_2-V_1)mk}$$

$$C_p = \frac{0.007154}{2*(0.55-(-0.1))*0.0223*0.01}$$

$$C_p = 24.72 \text{ F/g}$$
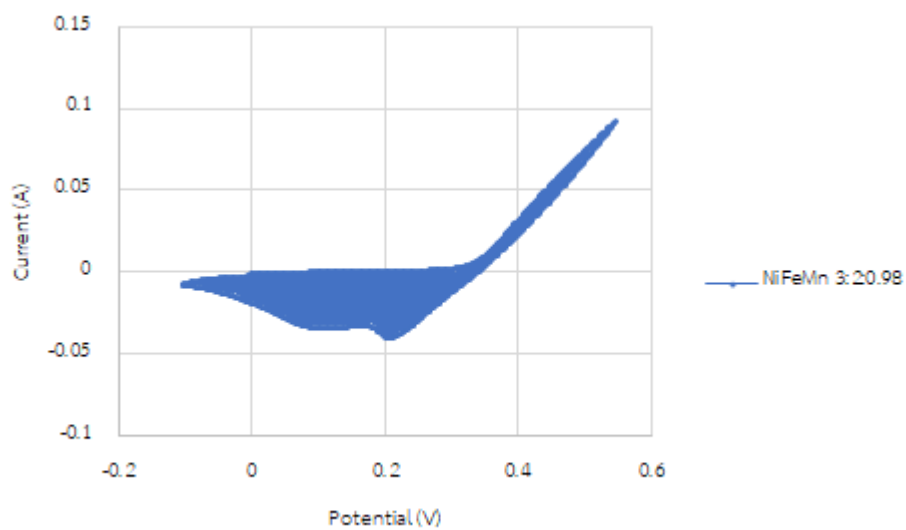
Figure 6.7 The 2nd cyclic voltammogram of NiFeMn LDH 3: 2: 0.98

Area = 0.01172 AV

LDH mass (active mass) = 0.0186 g

Scan rate = 0.01 V/s

$$C_p = \frac{A}{2(V_2-V_1)mk}$$

$$C_p = \frac{0.01172}{2*(0.55-(-0.1))*0.0186*0.01}$$

$$C_p = 48.57 \text{ F/g}$$
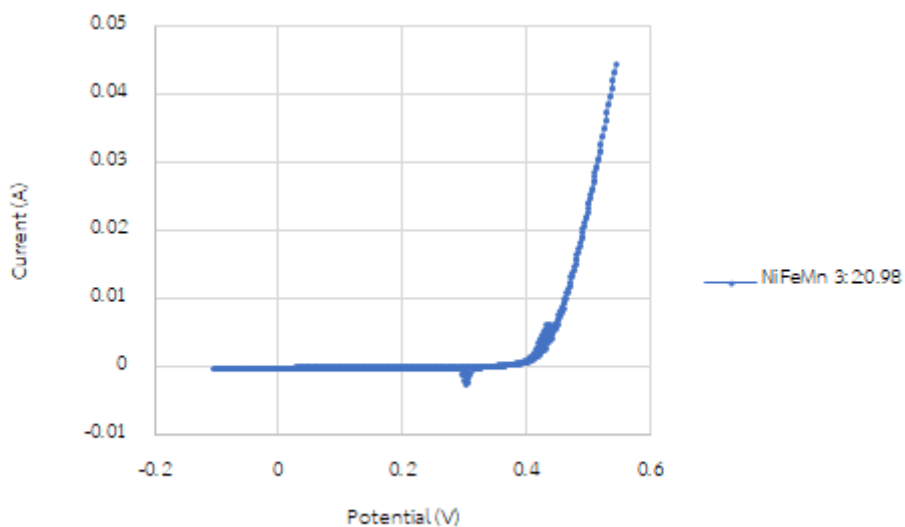
Figure 6.8 The 2nd cyclic voltammogram of NiFeMn LDH 3: 2: 1.7

Area = 0.01103 AV

LDH mass (active mass) = 0.0185 g

Scan rate = 0.01 V/s

$$C_p = \frac{A}{2(V_2-V_1)mk}$$

$$C_p = \frac{0.01103}{2*(0.55-(-0.1))*0.0185*0.01}$$

$$C_p = 45.86 \text{ F/g}$$

Figure 6.9 The 2nd cyclic voltammogram of NiMn LDH

Area = 0.01238 AV

LDH mass (active mass) = 0.0193 g

Scan rate = 0.01 V/s

$$C_p = \frac{A}{2(V_2 - V_1)mk}$$

$$C_p = \frac{0.01238}{2*(0.55-(-0.1))*0.0193*0.01}$$

$$C_p = 49.38 \text{ F/g}$$

130th cycle
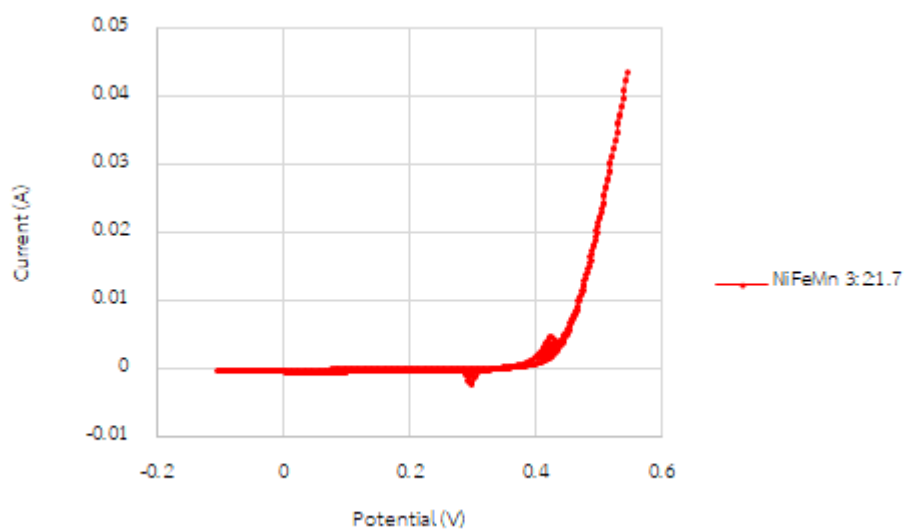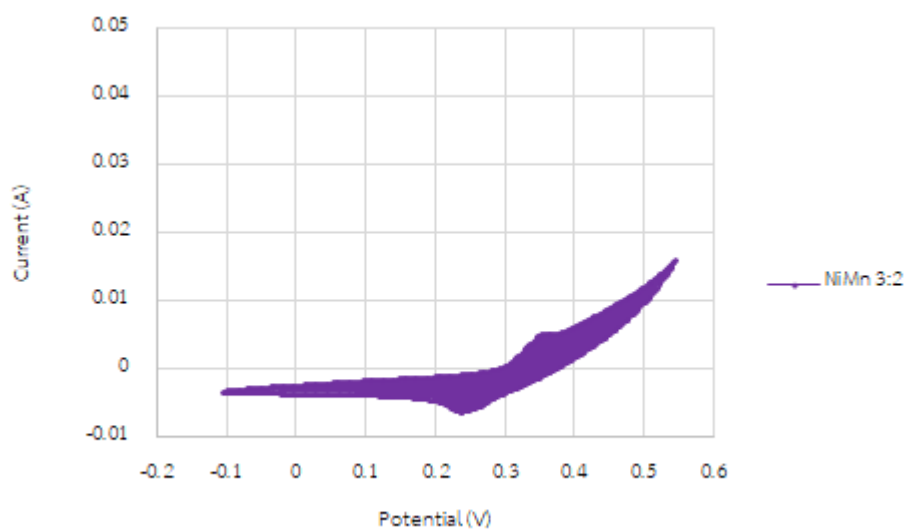

Figure 6.10 The 130th cyclic voltammogram of NiFe LDH

Area = 0.0001529 AV

LDH mass (active mass) = 0.0223 g

Scan rate = 0.01 V/s

$$C_p = \frac{A}{2(V_2-V_1)mk}$$

$$C_p = \frac{0.0001529}{2*(0.55-(-0.1))*0.0223*0.01}$$

$$C_p = 0.5283 \text{ F/g}$$

Figure 6.11 The 130th cyclic voltammogram of NiFeMn LDH 3: 2: 0.98

Area = 0.0002318 AV

LDH mass (active mass) = 0.0186 g

Scan rate = 0.01 V/s

$$C_p = \frac{A}{2(V_2 - V_1)mk}$$

$$C_p = \frac{0.0002318}{2*(0.55-(-0.1))*0.0186*0.01}$$

$$C_p = 0.9602 \text{ F/g}$$

Figure 6.12 The 130th cyclic voltammogram of NiFeMn LDH 3: 2: 1.7

Area = 0.0002759 AV

LDH mass (active mass) = 0.0185 g

Scan rate = 0.01 V/s

$$C_p = \frac{A}{2(V_2\text{-}V_1)mk}$$

$$C_p = \frac{0.0002759}{2*(0.55\text{-}(\text{-}0.1))*0.0185*0.01}$$

$$C_p = 1.147 \text{ F/g}$$

จุฬาลงกรณ์มหาวิทยาลัย

CHULALONGKORN UNIVERSITY

Figure 6.13 The 130th cyclic voltammogram of NiMn LDH

Area = 0.001834 AV

LDH mass (active mass) = 0.0193 g

Scan rate = 0.01 V/s

$$C_p = \frac{A}{2(V_2-V_1)mk}$$

$$C_p = \frac{0.001834}{2*(0.55-(-0.1))*0.0193*0.01}$$

$$C_p = 7.317 \text{ F/g}$$

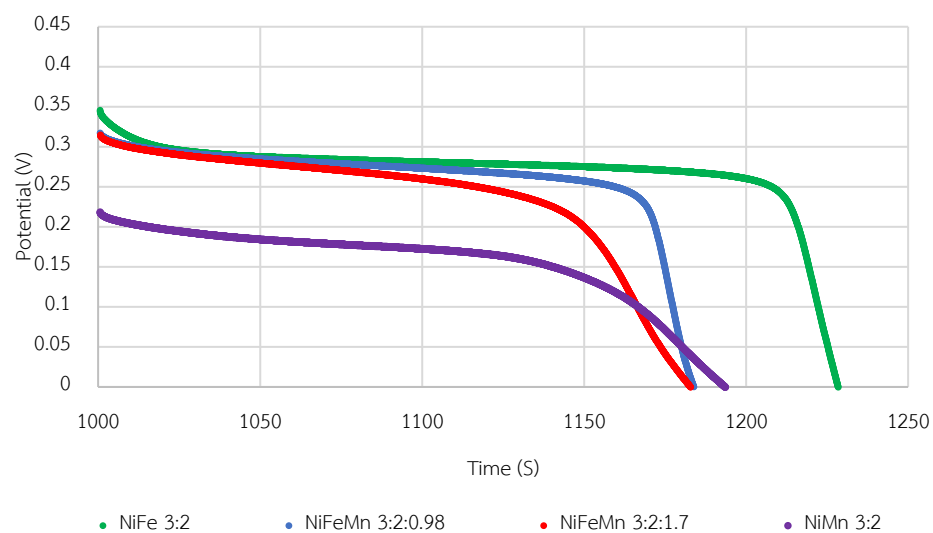Specific capacity from galvanostatic charge discharge was calculated as shown below.

1st cycle

Figure 6.14 The 1st galvanostatic charge discharge

NiFe LDH

t = 227.9 s

V = 0.3462 V

I/m = 0.1000 A/g

$$C_p = \frac{It}{m\Delta V}$$

$$C_p = \frac{0.1000*227.9}{0.3462}$$

C_p = 65.84 F/g

NiFeMn LDH 3: 2: 0.98

$t = 183.3$ s

$V = 0.3175$ V

$I/m = 0.1000$ A/g

$$C_p = \frac{It}{m\Delta V}$$

$$C_p = \frac{0.1000*183.3}{0.3175}$$

$C_p = 57.73$ F/g

NiFeMn LDH 3: 2: 1.7

$t = 182.2$ s

$V = 0.3153$ V

$I/m = 0.1000$ A/g

$$C_p = \frac{It}{m\Delta V}$$

$$C_p = \frac{0.1000*182.2}{0.3153}$$

$C_p = 57.79$ F/g

NiMn LDH

$t = 193.0$ s

$V = 0.2187$ V

$I/m = 0.1000$ A/g

$$C_p = \frac{It}{m\Delta V}$$

$$C_p = \frac{0.1000*193.0}{0.2187}$$

$C_p = 88.25$ F/g

5th cycle
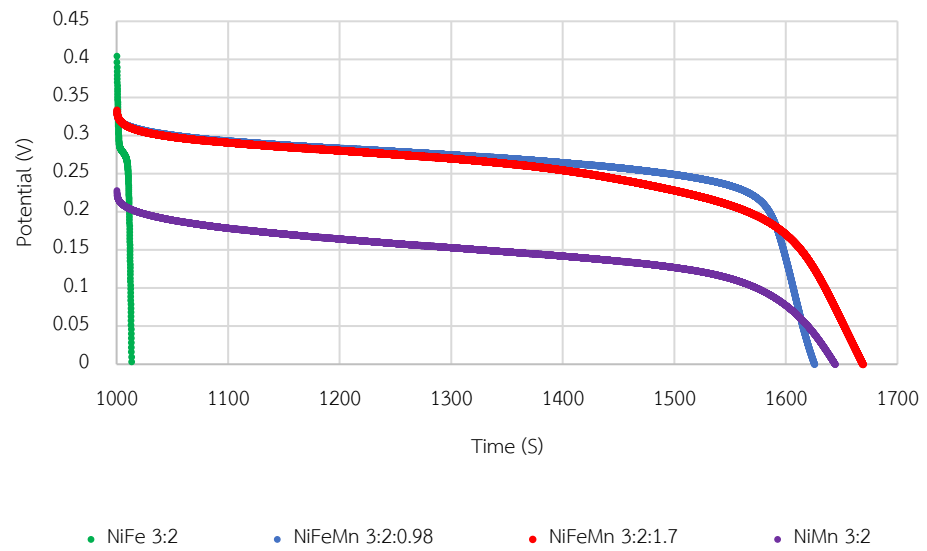
Figure 6.15 The 5th galvanostatic charge discharge

NiFe LDH

$$t = 13.10 \text{ s}$$

$$V = 0.4049 \text{ V}$$

$$I/m = 0.1000 \text{ A/g}$$

$$C_p = \frac{It}{m\Delta V}$$

$$C_p = \frac{0.1000*13.10}{0.4049}$$

$$C_p = 3.24 \text{ F/g}$$

NiFeMn LDH 3: 2: 0.98

$t = 625.4$ s

$V = 0.3317$ V

$I/m = 0.1000$ A/g

$$C_p = \frac{It}{m\Delta V}$$

$$C_p = \frac{0.1000 \ast 625.4}{0.3317}$$

$C_p = 188.5$ F/g

NiFeMn LDH 3: 2: 1.7

$t = 668.8$ s

$V = 0.3338$ V

$I/m = 0.1000$ A/g

$$C_p = \frac{It}{m\Delta V}$$

$$C_p = \frac{0.1000 \ast 668.8}{0.3338}$$

$C_p = 200.4$ F/g

NiMn LDH

$t = 643.9$ s

$V = 0.2283$ V

$I/m = 0.1000$ A/g

$$C_p = \frac{It}{m\Delta V}$$

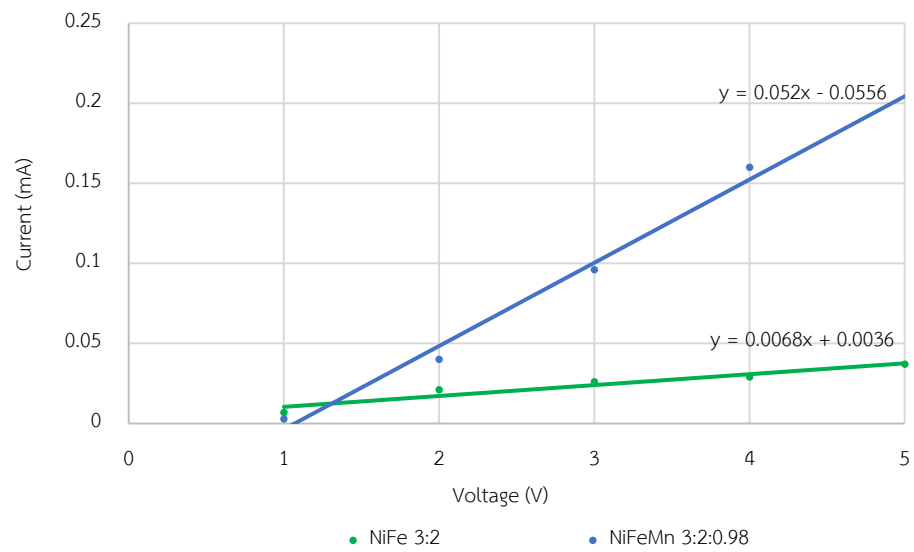$$C_p = \frac{0.1000 \ast 643.9}{0.2283}$$

$C_p = 282.0$ F/g

Figure 6.16 Current voltage relationship

NiFe LDH

slope = 0.0068 mA/V

L = length = LDH pellet thickness = 1.617 mm

A = surface area = $2\pi r^2 = 2\pi(6.25)^2$ = 245.54 cm^2

$V = IR$

$R = \dfrac{\Delta V}{\Delta I} = \dfrac{1}{slope}$

$R = \dfrac{1}{0.0068}$

R = 147.1 kΩ

$R = \dfrac{\rho L}{A}$

$\rho = \dfrac{RA}{L}$

$\rho = \dfrac{147.1 \times 245.54}{1.617}$

ρ = 2.23x10^6 Ωm

NiFeMn LDH 3: 2: 098

slope = 0.052 mA/V

L = length = LDH pellet thickness = 1.712 mm

A = surface area = $2\pi r^2 = 2\pi(6.25)^2 = 245.54$ cm^2

$V = IR$

$$R = \frac{\Delta V}{\Delta I} = \frac{1}{slope}$$

$$R = \frac{1}{0.052}$$

$R = 19.23$ kΩ

$$R = \frac{\rho L}{A}$$

$$\rho = \frac{RA}{L}$$

$$\rho = \frac{19.23 \times 245.54}{1.712}$$

$\rho = 2.76 \times 10^5$ Ωm

The resistance data from EIS were evaluated by Nova2.1.2

NiFe LDH : R_s = 889.9 Ω, R_{ct} = 4102 Ω
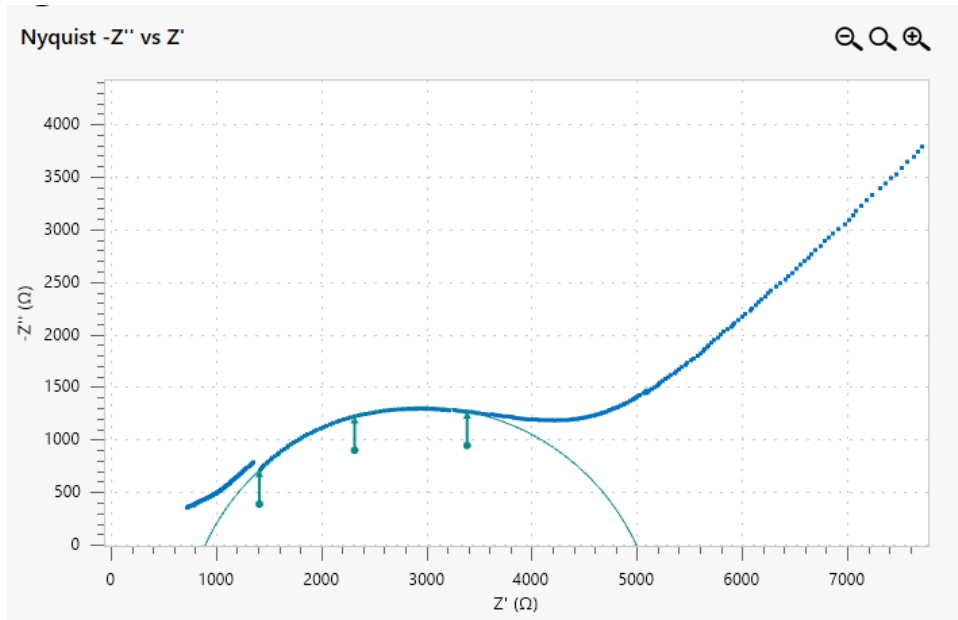

Figure 6.17 The Nyquist plot of NiFe LDH

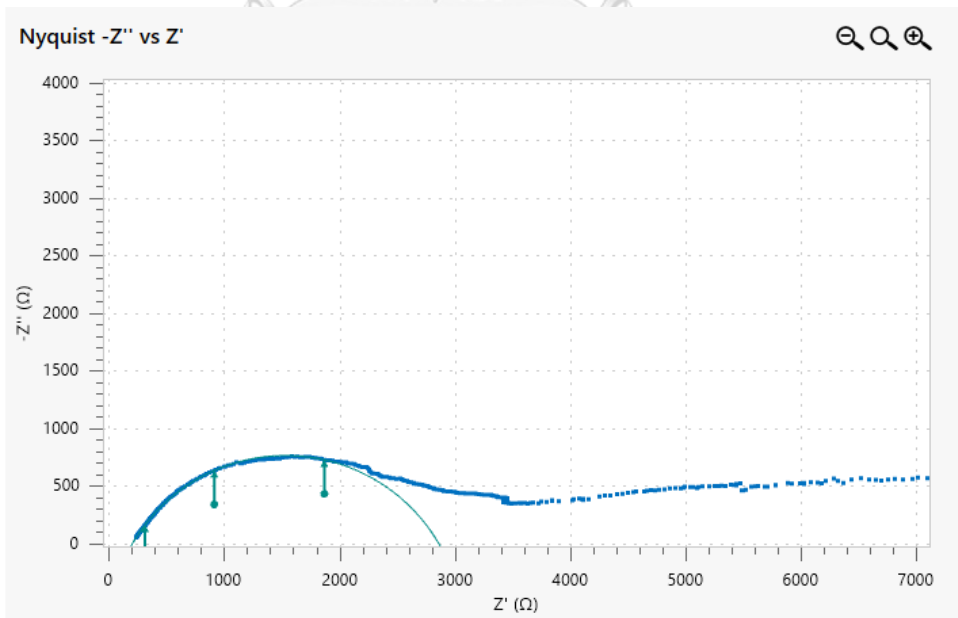NiFeMn LDH 3: 2: 098 : R_s = 197.3 Ω, R_{ct} = 2661 Ω

Figure 6.18 The Nyquist plot of NiFeMn LDH 3: 2: 098
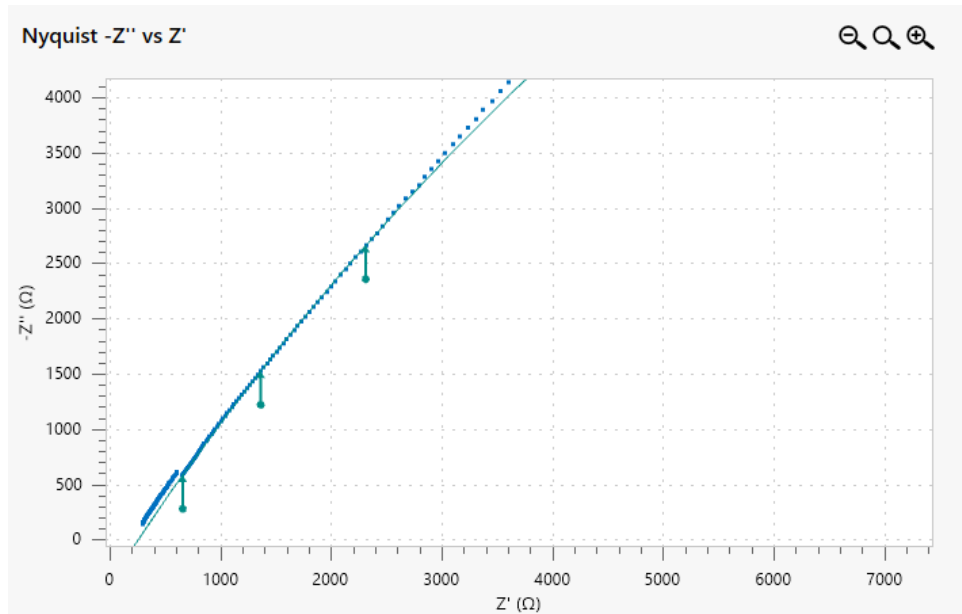
NiFeMn LDH 3: 2: 1.7 : R_s = 169.2 Ω, R_{ct} = NA

Figure 6.19 The Nyquist plot of NiFeMn LDH 3: 2: 1.7
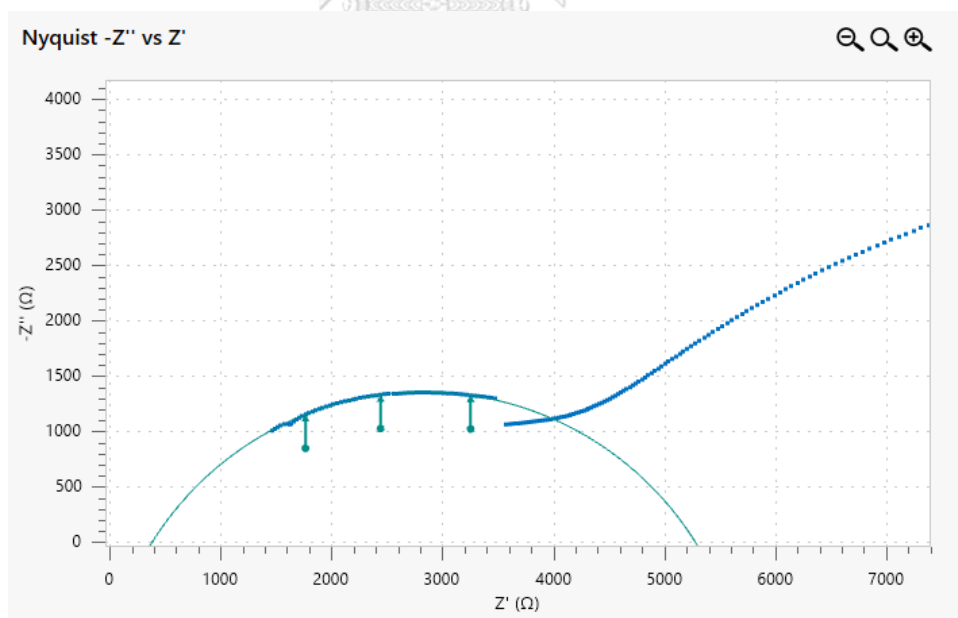
NiMn LDH: R_s = 375.0 Ω, R_{ct} = 4903 Ω

Figure 6.20 The Nyquist plot of NiMn LDH

VITA

NAME   Machima Mongkhonratanachai

DATE OF BIRTH   17 November 1996

PLACE OF BIRTH   Bangkok

INSTITUTIONS ATTENDED Bachelor's Degree in Chemistry from Faculty of Science,
                          Chulalongkorn University in 2017

HOME ADDRESS   99/3 Chollada Suvannaphomi Village, Soi Ladkrabang54,
                          Ladkrabang Road, Srisajorrakhenoi Subdistrict,
                          Bangsaothong District, Samutprakran 10540

PUBLICATION   Poster presentation on the topic of "Synthesis of
                          Manganese Doped Nickel Iron Layered Double Hydroxides
                          to Enhance Electrochemical Properties for
                          Supercapacitor", The 27th PPC Symposium on Petroleum,
                          Petrochemicals, and Polymers and The 12th Research
                          Symposium on Petrochemical and Materials Technology, 1
                          July 2021, Online.

AWARD RECEIVED   Thailand's nominate to attend Global Young Scientist
                          Summit 2022